



HAL
open science

Enhanced and non-monotonic effective kinetics of solute pulses under Michaelis–Menten reactions

Antoine Hubert, Tomás Aquino, Hervé Tabuteau, Yves Méheust, Tanguy Le Borgne

► **To cite this version:**

Antoine Hubert, Tomás Aquino, Hervé Tabuteau, Yves Méheust, Tanguy Le Borgne. Enhanced and non-monotonic effective kinetics of solute pulses under Michaelis–Menten reactions. *Advances in Water Resources*, 2020, 146, pp.103739. 10.1016/j.advwatres.2020.103739 . insu-02935685

HAL Id: insu-02935685

<https://insu.hal.science/insu-02935685>

Submitted on 10 Sep 2020

HAL is a multi-disciplinary open access archive for the deposit and dissemination of scientific research documents, whether they are published or not. The documents may come from teaching and research institutions in France or abroad, or from public or private research centers.

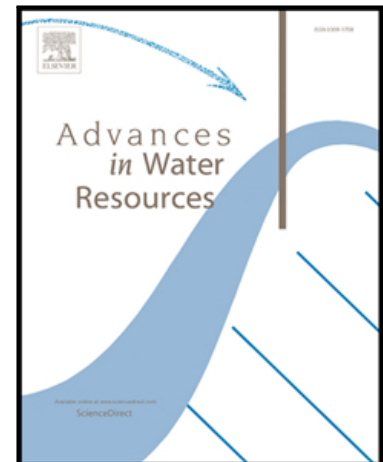
L'archive ouverte pluridisciplinaire **HAL**, est destinée au dépôt et à la diffusion de documents scientifiques de niveau recherche, publiés ou non, émanant des établissements d'enseignement et de recherche français ou étrangers, des laboratoires publics ou privés.

Journal Pre-proof

Enhanced and non-monotonic effective kinetics of solute pulses under Michaelis–Menten reactions

Antoine Hubert, Tomás Aquino, Hervé Tabuteau, Yves Méheust, Tanguy Le Borgne

PII: S0309-1708(20)30375-4
DOI: <https://doi.org/10.1016/j.advwatres.2020.103739>
Reference: ADWR 103739



To appear in: *Advances in Water Resources*

Received date: 20 April 2020
Revised date: 20 July 2020
Accepted date: 14 August 2020

Please cite this article as: Antoine Hubert, Tomás Aquino, Hervé Tabuteau, Yves Méheust, Tanguy Le Borgne, Enhanced and non-monotonic effective kinetics of solute pulses under Michaelis–Menten reactions, *Advances in Water Resources* (2020), doi: <https://doi.org/10.1016/j.advwatres.2020.103739>

This is a PDF file of an article that has undergone enhancements after acceptance, such as the addition of a cover page and metadata, and formatting for readability, but it is not yet the definitive version of record. This version will undergo additional copyediting, typesetting and review before it is published in its final form, but we are providing this version to give early visibility of the article. Please note that, during the production process, errors may be discovered which could affect the content, and all legal disclaimers that apply to the journal pertain.

© 2020 Published by Elsevier Ltd.

Enhanced and non-monotonic effective kinetics of solute pulses under Michaelis–Menten reactions

Antoine Hubert^a, Tomás Aquino^a, Hervé Tabuteau^b, Yves Méheust^a, Tanguy Le Borgne^{a,*}

^a*Univ. Rennes, CNRS, Géosciences Rennes, UMR 6118, 35000 Rennes, France*

^b*Univ. Rennes, CNRS, Institut de Physique de Rennes, UMR 6251, 35000 Rennes, France*

Abstract

Michaelis–Menten kinetics describe a broad range of physical, chemical, and biological processes. Since they are non-linear, spatial averaging of reaction kinetics is non-trivial, and it is not known how concentration gradients affect the global effective kinetics. Here, we use numerical simulations and theoretical developments to investigate the effective kinetics of diffusing solute pulses locally subject to Michaelis–Menten reaction kinetics. We find that coupled diffusion and reaction lead to non-monotonic effective kinetics that differ significantly from the local kinetics. The resulting effective reaction rates can be significantly enhanced compared to those of homogeneous batch reactors. We uncover the different regimes of effective kinetics as a function of the Damköhler number and Michaelis–Menten parameters and derive a theory that explains and quantifies these upscaled kinetics using a weakly-coupled description of reaction and diffusion. We illustrate the consequences of these findings on the accelerated consumption of nutrient pulses by bacteria. These results are relevant to a large spectrum of reactive systems characterized by heterogeneous concentration landscapes.

Keywords: Michaelis–Menten, effective kinetics, solute pulses, concentration gradients, upscaling, bacteria uptake

*Corresponding author

Email address: tanguy.le-borgne@univ-rennes1.fr (Tanguy Le Borgne)

1 1. Introduction

2 Michaelis–Menten kinetics [1] occur in many natural and engineered reac-
3 tive systems. They were originally developed as a model of catalytic reactions,
4 where the reaction of interest is mediated by binding to a catalyst, leading to
5 saturation effects [1, 2]. This type of kinetics has found applicability in a variety
6 of contexts, such as microbial growth [3, 4], chemotaxis [5], solute transport in
7 biological tissues [6, 7, 8, 9], enzyme reactions [10], predator-prey models [11],
8 and reaction-diffusion in electrodes [12]. In the context of bacterial growth,
9 it is also known as Monod kinetics [13]. They have been used extensively to
10 model biodegradation of contaminants in hydrological and groundwater sys-
11 tems [14, 15, 16, 17, 18, 19]. These kinetics display a simple non-linearity:
12 the reaction rate is proportional to concentration at low concentrations and
13 saturates to a constant above a threshold concentration. Analytical solutions
14 exist for the Michaelis-Menten kinetics in batch conditions [20, 21]. For non-
15 homogeneous systems, the reaction-diffusion equation with Michaelis-Menten
16 kinetics has been analyzed mathematically for different applications, leading to
17 approximate solutions in some regimes [6, 7, 8, 22, 23, 24, 25, 26]. Here we
18 analyze the effect of chemical gradients on the average kinetic laws for local
19 Michaelis-Menten kinetics. We investigate whether non-homogeneities in con-
20 centrations may lead to enhanced or reduced average reaction rates compared
21 with batch kinetics, characterized by homogeneous concentrations.

22 Under non-linear kinetics, unresolved concentration gradients lead to effec-
23 tive macroscopic reactive transport laws that are different from microscopic
24 laws [27, 28, 29, 30]. In the context of Michaelis-Menten reactions, the effect
25 of mass transfer limitations on effective macroscopic kinetics has been studied
26 with an emphasis on bioavailability limitations when micro-organisms are lo-
27 cated on solid surfaces [31, 32, 33] or more generally distributed in space [34].
28 Mixing limitation with Michaelis–Menten kinetics have also been investigated
29 in the context of reactive fronts, where reactants are spatially segregated and
30 mixing is the limiting step to bring reactants into contact [35, 36]. Here we

31 study situations where nutrients or reactants are released as discrete pulses in
32 time and space, which encompasses a large spectrum of natural and engineered
33 systems. Examples include pulse of nutrients in soil [37, 38], plants [39], aquifers
34 [40] or catchments [41], which are often consumed by biological agents through
35 Michaelis–Menten kinetics [42]. While other types of non-homogeneous initial
36 conditions could be considered, we argue that the general impact of concentra-
37 tion gradients on the average kinetics will be similar as for pulses.

38 We study the effective kinetics of diffusing pulses of a single chemical species
39 undergoing degradation with Michaelis–Menten kinetics. We assume that the
40 local kinetics are uniform in space and hence focus on the effect of spatial
41 and temporal changes in reactant concentration on the effective kinetics. We
42 approximate these nonlinear kinetics by a sharp crossover from a linear depen-
43 dency of the degradation rate on c for concentrations lower than the crossover
44 concentration, to a saturated, constant rate above it. We investigate the de-
45 pendency of the effective kinetics on the Damköhler number Da and the ratio
46 α between the kinetics' crossover concentration and the initial concentration.
47 We develop a semi-analytical framework relying on a weak-coupling approx-
48 imation regarding diffusion and reaction. The results compare favorably to
49 numerical simulations of the coupled equations. Fully-analytical descriptions
50 are also derived for asymptotic regimes corresponding respectively to reaction-
51 and diffusion-dominated dynamics.

52 In the following, we first present, in Section 2, a mathematical description
53 of the dynamics, including the solution under well-mixed conditions, which will
54 serve as the reference scenario. Next, Section 3 is concerned with analysing the
55 dynamics of the effective reaction rate as a function of the Damköhler number
56 and α based on numerical simulations. Section 4 is devoted to the derivation
57 of the semi-analytical theory relying on the approximation of weakly-coupled
58 diffusion and reaction. Section 5 explores the consequences of our results in
59 the context of the consumption of nutrients by bacteria. Conclusions are drawn
60 and the results discussed in terms of their relevance to natural systems in sec-
61 tion 6. Additional technical derivations regarding the analytical theory and

62 details on the performance of the weakly coupled approximation may be found
63 in appendix.

64 2. Dynamics

65 The dependence of local reaction rate on local concentration associated with
66 Michaelis–Menten kinetics is given by

$$r'(c') = \frac{\mu c'}{K + c'}, \quad (1)$$

67 where c' is the concentration, μ is the maximum reaction rate per unit con-
68 centration, and K is the characteristic concentration for the transition between
69 first-order and zero-order kinetics. The key qualitative features of these kinetics
70 are (i) saturation of the reaction rate at high concentrations $c' \gg K$, and (ii)
71 linear growth of the reaction rate at low concentrations $c' \ll K$.

72 We define the normalized concentration and characteristic concentrations
73 respectively as

$$c = c'/c'_0 \quad (2)$$

74 and

$$\alpha = K/c'_0, \quad (3)$$

75 where c'_0 is the initial concentration. We associate a characteristic reaction time
76 with the low-concentration regime,

$$\tau_\ell = K/\mu, \quad (4)$$

77 and we nondimensionalize time as

$$t = t'/\tau_\ell. \quad (5)$$

78 This leads to a dimensionless reaction rate $r = \tau_\ell r'/c'_0$, given as a function of
79 dimensionless concentration by

$$r(c) = \frac{\alpha c}{\alpha + c}. \quad (6)$$

80 In nondimensional terms, the saturation condition reads $c \gg \alpha$, and the satu-
 81 rated rate value is likewise given by $r(c) = \alpha$. In the following, we present and
 82 discuss our results in terms of nondimensional quantities, unless noted other-
 83 wise.

84 For simplicity, in order to elucidate the main mechanisms driving the effec-
 85 tive kinetics describing the evolution of total mass under this type of scenario,
 86 we consider a piecewise-linear model of kinetics accounting for saturation,

$$r(c) = cH(\alpha - c) + \alpha H(c - \alpha), \quad (7)$$

87 where H is the Heaviside step function. This corresponds to a linear increase,
 88 $r(c) = c$, of the reaction rate up to the critical concentration α , so that $r(\alpha) = \alpha$.
 89 Above the critical concentration, the reaction rate saturates and remains equal
 90 to its maximum value α (see Fig. 1). This model simplifies the analytical
 91 treatment, and allows us to focus on the key features of the interplay between
 92 transport-induced mixing and saturation. In Appendix F, we investigate nu-
 93 merically the effect of this simplification and show that it tends to slightly
 94 over-estimate the maximum effective reaction rates (Fig. F.16). However, re-
 95 sults are very similar since the piecewise-linear approximation is very close to
 96 the two regimes over orders of magnitudes in concentrations (Fig. 1 and F.17).

97 2.1. Well-mixed kinetics

98 We first consider the well-mixed case, corresponding to the conditions found
 99 in a batch reactor. The concentration c is then spatially homogeneous and
 100 depends only on time t . The dynamic equation describing concentration decay
 101 is the well-mixed rate law

$$\dot{c} = -r(c), \quad (8)$$

102 which describes the decay resulting from the sharp crossover approximation of
 103 the Michaelis–Menten kinetics when the rate $r(c)$ is defined according to Eq. (7).
 104 Throughout, the dot denotes (nondimensional-time) differentiation.

105 If the initial concentration is sufficiently large ($\alpha < 1$), reaction starts in
 106 the saturated regime. The reaction then proceeds at a constant rate for a

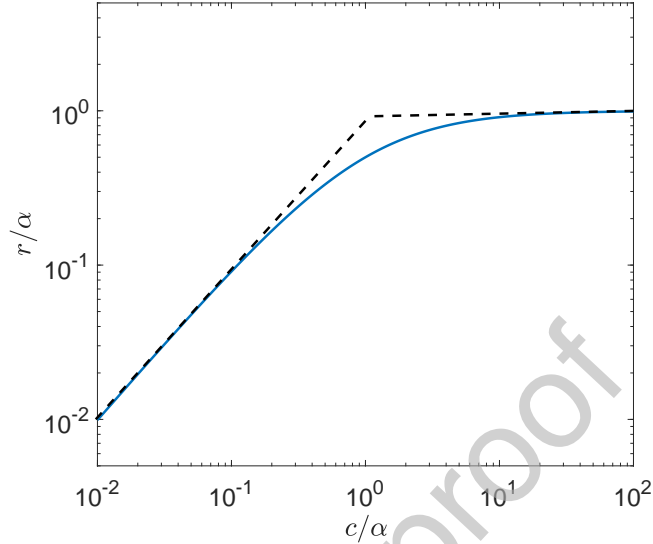


Figure 1: Nonlinear kinetics exhibiting saturation. Blue: Michaelis–Menten kinetics, Eq. (6). Black dashed: Piecewise-linear kinetics, Eq. (7).

107 dimensionless duration σ_B , defined such that $c(\sigma_B) = \alpha$. For $\alpha > 1$, the batch
 108 starts in the linear regime and $\sigma_B = 0$. Thus,

$$\sigma_B = \max \left\{ 0, \frac{1 - \alpha}{\alpha} \right\}. \quad (9)$$

109 For $t > \sigma_B$, standard linear dynamics apply, and the concentration decreases
 110 exponentially. The total mass corresponding to a homogeneous batch of width
 111 s_0 is given, in one dimension, by $M'_B(t) = s_0 c'(t)$, which we nondimensionalize
 112 as $M_B(t) = M'_B(t)/M'_B(t=0)$. Hence, expressed in nondimensional terms, the
 113 temporal evolution of the total mass of reactant is given by

$$M_B(t) = \begin{cases} 1 - \alpha t, & t \leq \sigma_B \\ \min\{\alpha, 1\} e^{-(t-\sigma_B)}, & t > \sigma_B \end{cases}. \quad (10)$$

114 2.2. Diffusing pulses of reactive solutes

115 We now consider a pulse of a reactant diffusing in a solution and locally
 116 subject to the piecewise-linear reaction rate $r(c)$ defined in Eq. (7). Our goal

117 is to compare the effective reaction kinetics under these conditions to the well-
 118 mixed batch reaction kinetics for the same initial mass of reactant and the
 119 same initial concentration. For simplicity, we consider transport in one spatial
 120 dimension, but the approach can be extended to three dimensions. The initial
 121 condition is taken to be homogeneous within a region of width s_0 , centered at
 122 $x' = 0$. For a total initial mass of M'_0 , the initial concentration corresponding to
 123 this injection is $c'_0 = M'_0/s_0$. In dimensional terms, the corresponding dynamical
 124 equation is

$$\partial_t c' = D \partial_x^2 c' - r'(c'), \quad (11)$$

125 where D is the diffusion coefficient. Here and throughout, the notation ∂_y de-
 126 notes the partial derivative with respect to a variable y . Note that equation
 127 (11) is also relevant for one-dimensional dispersion when substituting the diffu-
 128 sion coefficient by a dispersion coefficient. Hence results derived here for one-
 129 dimensional diffusion also apply to one-dimensional dispersion, which would be
 130 relevant for instance for reactive pulses released in porous media columns under
 131 flow [43]. In Appendix G we also discuss the effect of dimensionality by solving
 132 the reactive transport equation in spherical coordinate for three-dimensional
 133 diffusion. Since the surface available for diffusion is larger in three-dimensions,
 134 the effect of average kinetics enhancement is found to be even more pronounced
 135 for three-dimensional pulses than for one-dimensional pulses (Fig. G.18 and
 136 G.19).

137 As above, we nondimensionalize concentration as $c = c'/c'_0$ and time as
 138 $t = t'/\tau_\ell$. Furthermore, we normalize position as $x = x'/s_0$. We introduce
 139 also the diffusion time $\tau_D = s_0^2/(2D)$, corresponding to the characteristic time
 140 needed to homogenize the width of the initial condition, i.e., to homogenize a
 141 unit length in dimensionless units. We then define the Damköhler number as

$$\text{Da} = \frac{\tau_D}{\tau_\ell} = \frac{s_0^2 \mu}{2DK}, \quad (12)$$

142 which quantifies the relative importance of reaction versus diffusion and is also
 143 simply the diffusion time in dimensionless units. The dynamical equation then

144 becomes

$$\partial_t c = \frac{\partial_x^2 c}{2\text{Da}} - r(c), \quad (13)$$

145 where $r(c)$ is given by equation (7) and the initial condition is

$$c(x, 0) = H(x + 1/2)H(1/2 - x). \quad (14)$$

146 Since under diffusion and degradation the maximum concentration cannot
 147 increase, once the latter reaches the value α the kinetics become linear every-
 148 where and are identical to the well-mixed scenario. Similarly to above, we denote
 149 by σ the time at which the maximum concentration reaches α . For $t \geq \sigma$, we
 150 have

$$M(t) = M(\sigma)e^{-(t-\sigma)} \quad (15)$$

151 and

$$\dot{M}(t) = -M(\sigma)e^{-(t-\sigma)}. \quad (16)$$

152 As for the batch problem, $\alpha > 1$ means all mass starts in the linear regime,
 153 corresponding to the linear reaction problem for all times. Furthermore, for any
 154 value of α , the limit $\text{Da} \rightarrow \infty$ reduces to the batch problem. This happens
 155 because, in this limit, all mass reaches the linear regime through reaction before
 156 diffusion has time to deform the initial uniform concentration distribution. Note
 157 that we consider a pulse in a formally infinite domain. This means that our
 158 results for the total mass are valid so long as deformation of the pulse by diffusion
 159 does not extend to the spatial domain boundaries, at least while the saturated
 160 regime lasts. In a finite domain, the limit $\text{Da} \rightarrow 0$ reduces to a batch of the size
 161 of the domain (as opposed to the initial pulse size), corresponding to the initial
 162 pulse becoming homogeneous over the entire domain before reaction becomes
 163 important.

164 2.3. Effective kinetics of diffusing pulses

165 In order to quantify the effective kinetics of diffusing pulses, we study the
 166 evolution of the total mass of reactant. In dimensionless terms, the effective

167 reaction rate as a function of time is given by

$$r_t(t) = -\dot{M}(t). \quad (17)$$

168 We analyze the evolution of the effective reaction rate r_t as a function of time
169 and as a function r_M of the mass itself,

$$r_M(m) = -\dot{M}[T(m)], \quad (18)$$

170 where $T(m)$ is the time at which the total mass $M[t = T(m)]$ is equal to m .
171 Under well-mixed conditions, the effective kinetics governing the total mass
172 always coincide with the local kinetics, irrespective of the latter. In the pulse
173 scenario and for nonlinear kinetics, however, the mixing state, as encoded in
174 the concentration profile, changes the nature of the effective reaction rate. As
175 we will see, this is reflected in a qualitatively different behavior of $r_M(m)$ when
176 compared to the local kinetics $r(c)$ seen as a function of concentration.

177 Note that, formally, T is the inverse of M , that is, $M[T(m)] = m$ and
178 $T[M(t)] = t$. This inverse exists for our problem because the mass as a function
179 of time is monotonic for degradation kinetics, meaning that a value of mass
180 corresponds to exactly one value of time and vice-versa. If this were not the case,
181 multiple rates would be associated with a given value of mass, and the effective
182 kinetics would exhibit hysteresis. We do not address this type of scenario in the
183 present work.

184 3. Numerical simulations

185 Before proceeding with the theoretical discussion, we illustrate some key
186 aspects of the dynamics using numerical simulations. To this end, we numeri-
187 cally integrated Eq. (13) with a square pulse initial condition, as described in
188 Section 2.2, using Matlab's *pdepe* method.

189 Figure 2 illustrates the evolution of the concentration profile for all com-
190 binations of values of $\text{Da} \in \{10^{-3}, 1, 10^3\}$ and $\alpha \in \{0.01, 0.05, 0.26\}$. These
191 parameter combinations are representative of the different qualitative dynamics

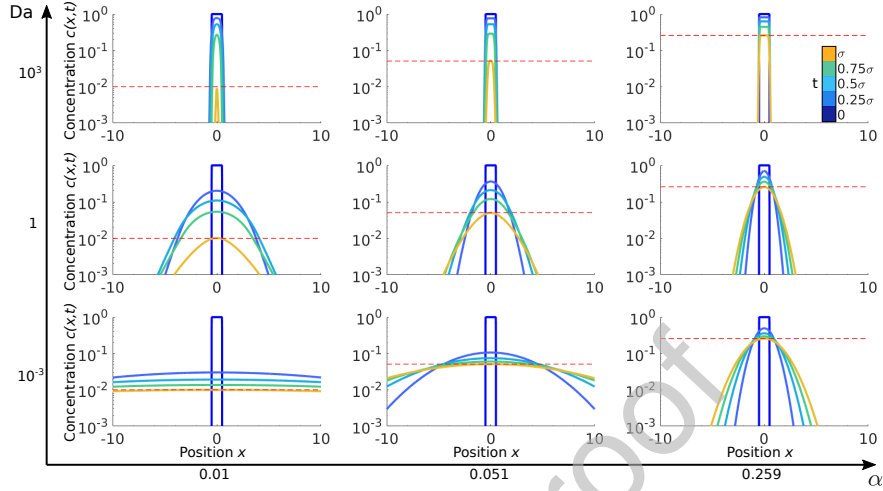


Figure 2: Temporal evolution of the concentration profile for a square-pulse initial condition, for varying Damköhler number Da and maximum batch rate α . Five evenly-spaced times between $t = 0$ and $t = \sigma$ are represented by color-coded profiles. The value of α is shown as a dashed red line.

192 which may be observed. For high Da and high α (top right panel), reaction
 193 dominates over diffusion and the shape of the initial profile remains relatively
 194 unchanged until the onset of the linear regime. In fact, this is expected for
 195 sufficiently high Da , whatever the value of α . Indeed, in the limit of high Da ,
 196 diffusion becomes slow compared to reaction, so that each region of the pulse
 197 becomes essentially independent, and the pulse behaves as a set of independent
 198 batches. Hence, for sufficiently high Da and a square pulse initial condition, the
 199 pulse remains homogeneous for the duration of the saturated regime and the ef-
 200 fective kinetics tend towards the batch kinetics. For low Da and high α (bottom
 201 right), diffusion dominates and the profile approaches a Gaussian before relevant
 202 reaction occurs. For decreasing α and increasing Da (left and center panels),
 203 corresponding to an initial condition higher above the saturation threshold and
 204 faster reaction, there is an enhanced interplay between diffusion and reaction,
 205 and the evolution of the concentration profile becomes more complex.

206 Figure 3a compares the evolution of the total mass over time for diffusing

207 pulses and well-mixed batch conditions. The interplay between diffusion and
 208 nonlinear reaction in pulses leads to an enhancement of the effective reaction
 209 rate when compared to the batch reaction. The well-mixed conditions are the
 210 least efficient, in the sense that the remaining mass is always higher at a given
 211 time. This is consistent with the above discussion regarding the convergence
 212 to batch behavior at high Da . For low Da , when the effect of diffusion is most
 213 pronounced, the effective reaction rate initially increases with time to reach
 214 a maximum before decaying at larger times (Fig. 3b). These non-monotonic
 215 effective kinetics contrast with the well-mixed scenario, which mimics the local
 216 kinetics (constant rate followed by exponential decay, see Eq. (16)).

217 Figure 3c compares the evolution of the effective reaction rate as a function
 218 of total mass with the local kinetics. The initial value of the reaction rate,
 219 corresponding to $M = 1$, is always the same as the initial batch reaction rate,
 220 because the initial conditions are identical. Then, the reaction rate increases
 221 up to a maximum value, before decreasing and reaching the linear regime when
 222 the peak concentration drops below α . The maximum reaction rates increase
 223 markedly with decreasing Da , and the local kinetics are recovered at high Da .
 224 Note that the reaction rate is maximum when the mass of the pulse is distributed
 225 such that all concentrations lie below α . Local concentrations then obey $\dot{c} = -c$,
 226 which upon spatial integration leads to $\dot{M} = -M$. This linear dependence
 227 corresponds to the upper envelope of $r_M(m)$, as seen in Fig. 3c. In Appendix A,
 228 we present a series of additional numerical simulations and discuss the sensitivity
 229 of the non-monotonic effective kinetics on Da and α (Fig. A.11).

230 The maximum reaction rate r_{\max} increases with decreasing Da and increasing
 231 α (Fig. 4a). Therefore, the region of maximum reaction rate corresponds to a
 232 regime where diffusion dominates over reaction and where the linear regime
 233 dominates over the saturated regime for most of the dynamics (see Fig. 1). The
 234 time t_{\max} at which this maximum reaction rate occurs is largest for high Da and
 235 low α , which corresponds to relatively low values of r_{\max} , see Fig. 4b. Note that
 236 α corresponds to the maximum reaction rate for well-mixed batch dynamics.
 237 Thus, increasing α leads to an increase in r_{\max} , but also in the maximum batch

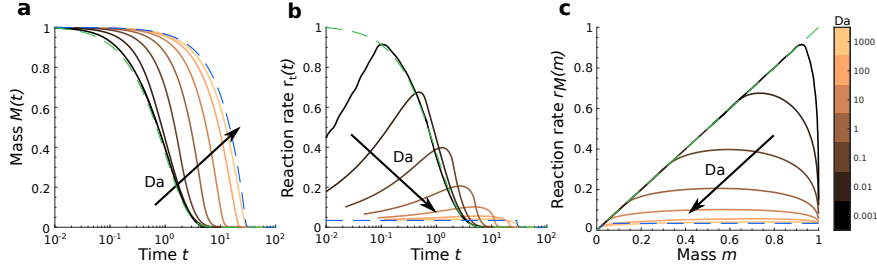


Figure 3: Total mass and effective reaction rate for varying Damköhler number Da and $\alpha = 0.05$ for a square initial condition. The well-mixed batch behavior is shown as dashed blue lines. The dashed green line corresponds to linear kinetics. **(a)** Time-evolution of the total mass. **(b)** Time-evolution of the effective reaction rate. Note that, due to the logarithmic time axis, the maximum rate is shifted with respect to the apparent maximum slope in panel (a). **(c)** Effective reaction rate as a function of total mass.

238 reaction rate.

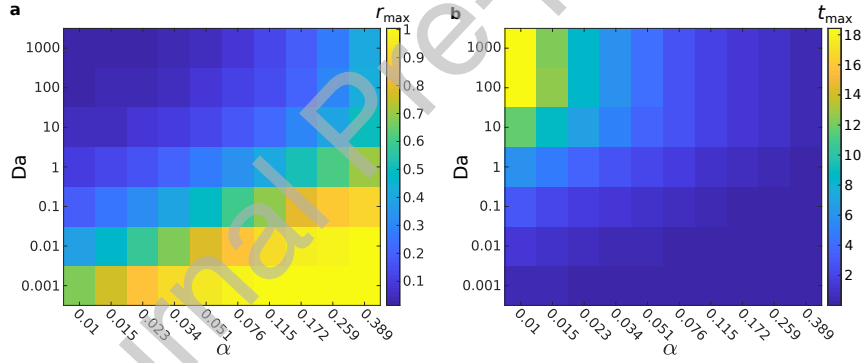


Figure 4: **(a)** Dependence of the maximum reaction rate r_{\max} on Da and α . **(b)** Similar results for the time t_{\max} at which the rate is maximum, $r_t(t_{\max}) = r_{\max}$.

239 To evaluate the reaction enhancement relative to the batch kinetics, we define
 240 the instantaneous reaction rate enhancement as

$$\tilde{r}(t) = \frac{\dot{M}(t)}{\dot{M}_B(t)}. \quad (19)$$

241 Because of the nature of Michaelis-Menten kinetics, the batch reaction rate
 242 $\dot{M}_B(t)$ is maximum at initial time and equal to α until the time $t = \sigma_B$ when
 243 the concentration reaches the transition concentration K . In contrast, the max-

244 imum reaction rate of the pulse kinetics $\dot{M}(t)$ is always maximum at an in-
 245 termediate time $t_{\max} < \sigma_B$ (Fig. 3). Hence the maximum reaction rate en-
 246 hancement is $\tilde{r}_{\max} = \dot{M}(t_{\max})/\alpha$ (Fig. 5). The maximum enhancement of the
 247 effective reaction is found in the limit of low Da and α . This corresponds to the
 248 case of diffusion processes dominating over reaction processes with a saturation
 249 concentration far below the initial concentration. Conversely, the minimum en-
 250 hancement of effective reaction by mixing is found in the opposite limit of high
 251 Da , where reaction dominates the dynamics, and high α . In [Appendix A](#),
 252 we present an analysis of the late time surviving masses to quantify the global
 253 reaction enhancement as a function of Da and α . The behavior of the global
 254 reaction enhancement follows the same tendencies as the instantaneous reaction
 255 enhancement (Fig. 5) described above: it is maximum for low Da and low α
 256 (Fig. [A.12](#)).

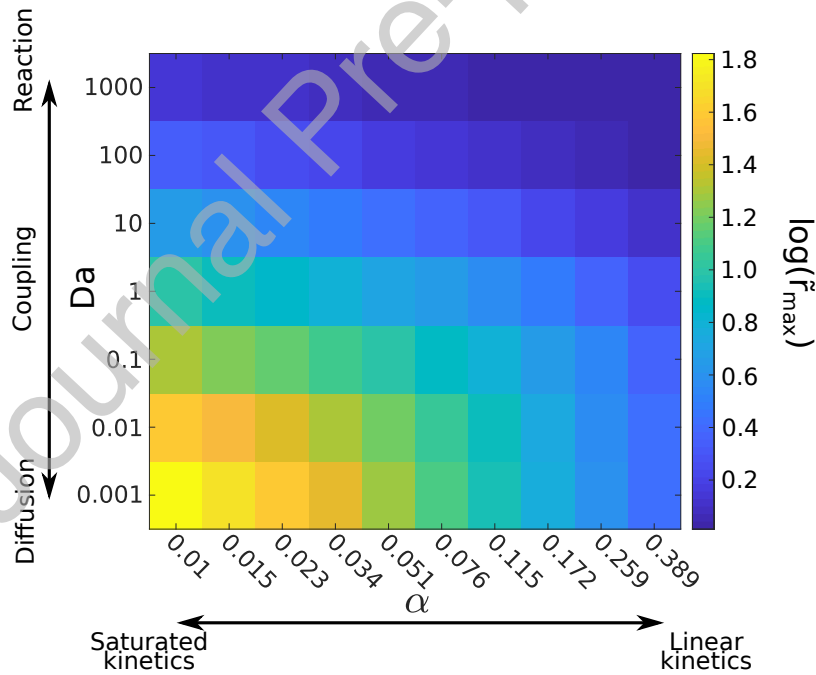


Figure 5: Dependence of the maximum reaction enhancement \tilde{r}_{\max} on Da and α .

257 **4. Theory**

258 We will now develop a theoretical description in order to better understand
 259 and quantify the numerical results discussed in the previous section. Since the
 260 dynamics for the mass are trivially identical to the batch problem whenever
 261 there is no saturated regime, we assume in what follows that the initial concen-
 262 tration maximum is larger than α . To develop the theory, we first introduce two
 263 key quantities governing the dynamics of the diffusion–reaction system, relat-
 264 ing to the dynamics of the spatial boundary between the linear and saturated
 265 kinetic regimes. We then develop a weak-coupling approximation to predict the
 266 evolution of total mass under reaction and diffusion.

267 *4.1. Transition between saturated and linear regimes*

268 For times $t < \sigma$, at which the peak concentration is above the saturation
 269 threshold α , the spatial domain may be divided into regions in which either the
 270 linear or the saturated reaction dynamics are taking place. In this framework,
 271 the first key quantity is the position of the interface between these domains. If
 272 the concentration profile is symmetric at the initial time, it will remain so at
 273 all times. If, further, over the half-space of positive x the initial concentration
 274 profile $c(x, t = 0)$ decreases monotonically (i.e., $\partial_x c < 0$ for $x > 0$), the profile
 275 will remain monotonically decreasing at all times. Hence, the saturated region
 276 occurs around $x = 0$, and is separated from the linear region by an interface
 277 at positions $\pm\xi(t)$, where $\xi(t)$ is the positive solution to $c[\xi(t), t] = \alpha$. We may
 278 thus separate the concentration field into two terms corresponding respectively
 279 to these two regions: $c(x, t) = c_\ell(x, t) + c_s(x, t)$, with

$$c_s(x, t) = c(x, t)H[\xi(t) - |x|], \quad c_\ell(x, t) = c(x, t)H[|x| - \xi(t)], \quad (20)$$

280 where s stands for saturated and ℓ for linear kinetics. The total mass is given
 281 by

$$M(t) = \int_{-\infty}^{\infty} dx c(x, t) = M_s(t) + M_\ell(t), \quad (21)$$

282 where the masses in each regime are given by the integrals of the corresponding
 283 concentrations.

284 The second key quantity is the total diffusive flux across the interface be-
 285 tween the regions (i.e., between reaction regimes). The net diffusive flux into
 286 the linear regime, considering the contributions at both $\pm\xi(t)$, is given by

$$f(t) = \frac{|\partial_x c(x, t)|_{x=\xi(t)}}{\text{Da}}. \quad (22)$$

287 For $t \geq \sigma$, when the full profile is in the linear reaction regime, we set $\xi(t) =$
 288 $f(t) = 0$. Then, $c(x, t) = c_\ell(x, t)$, and therefore $M(t) = M_\ell(t)$.

289 Mass transfer between regimes is governed by the direct effect of the diffusive
 290 flux across the interface, as well as by the displacement over time of the interface
 291 position due to both reaction and diffusion. By the Leibniz integral rule for
 292 differentiation under the integral sign, we have

$$\dot{M}_s(t) = \int_{|x| \leq \xi(t)} dx \partial_t c(x, t) + 2\alpha \dot{\xi}(t), \quad \dot{M}_\ell(t) = \int_{|x| > \xi(t)} dx \partial_t c(x, t) - 2\alpha \dot{\xi}(t). \quad (23)$$

293 The first term for each mass is due to the dynamical change of concentration,
 294 whereas the second is directly due to the time-dependence of the interface po-
 295 sition. As shown in [Appendix B](#), this leads to

$$M_s(t) = M_s(0) - R(t) - F(t) - B(t), \quad (24a)$$

$$M_\ell(t) = M_\ell(0)e^{-t} + G(t) + H(t), \quad (24b)$$

296 where

$$R(t) = 2\alpha \int_0^t du \xi(u), \quad (25a)$$

$$F(t) = \int_0^t du f(u) \quad (25b)$$

297 are the saturated-regime mass losses due respectively to reaction and diffusive
 298 flux at the boundaries,

$$B(t) = -2\alpha \int_0^t du \dot{\xi}(u) = 2\alpha[\xi(0) - \xi(t)] \quad (25c)$$

299 is the saturated mass loss due directly to the changing position of the interface,
 300 and

$$G(t) = \int_0^t du e^{-(t-u)} f(u), \quad (25d)$$

$$H(t) = -2\alpha \int_0^t du e^{-(t-u)} \dot{\xi}(u) \quad (25e)$$

301 correspond to the amount of mass which was transferred to the linear regime at
 302 some time $u < t$ by diffusion and directly by change of the interface position,
 303 respectively, and then survived (exponential) decay until time t .

304 In order to simplify the analytical treatment, it is convenient to consider
 305 a Gaussian initial condition. The role of the initial condition on the effective
 306 reaction kinetics will be discussed shortly. In dimensionless units, we consider
 307 an initial profile with unit mass and variance,

$$c(x, 0) = \exp(-x^2/2) / \sqrt{2\pi}. \quad (26)$$

308 Note that the corresponding initial masses are

$$M_s(0) = \operatorname{erf}[\xi(0)/\sqrt{2}], \quad M_\ell(0) = \operatorname{erfc}[\xi(0)/\sqrt{2}], \quad (27)$$

309 where erf and erfc are the error function and the complementary error function,
 310 respectively. The initial position of the interface is given by

$$\xi(0) = \sqrt{-\ln(2\pi\alpha^2)}. \quad (28)$$

311 The numerically-computed time evolution of the total mass and effective
 312 reaction rate for the Gaussian initial condition are shown in Fig. 6. For small Da ,
 313 when diffusion dominates, the behavior is the same as for the square-pulse initial
 314 condition because diffusion quickly deforms the initial profile into a Gaussian
 315 shape, before appreciable reaction takes place. In the limit of small Da , reaction
 316 approaches the linear regime for masses arbitrarily close to the initial mass. For
 317 high Da , however, the initial condition controls the kinetics, because diffusion
 318 cannot deform it substantially before the linear regime is reached. In this case,

319 reaction is much more efficient than for the batch scenario, since a relevant
 320 portion of the mass starts in the linear regime, whereas the well-mixed batch
 321 is fully saturated. This effect is more pronounced for low α , since, as discussed
 322 above, it corresponds to a longer duration of the saturated regime.

323 In what follows, we will develop approximations to quantitatively analyze
 324 the dynamical behavior of the diffusion–reaction system under the unit Gaussian
 325 initial condition. It should be kept in mind that the high-Da limit exhibits a be-
 326 havior which differs from the square-pulse initial condition, which, as discussed
 327 above, is identical with a well-mixed batch in this limit.

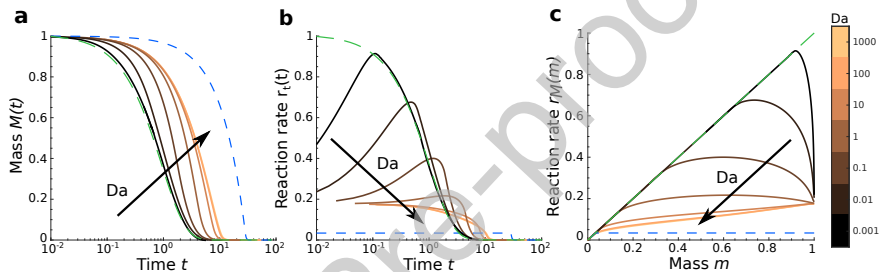


Figure 6: Total mass and reaction rate, computed numerically for the Gaussian initial condition. The maximum batch rate is $\alpha = 0.05$. The equivalent batch dynamics are shown as dashed blue lines. (a) Time evolution of total mass. (b) Time evolution of the reaction rate. (c) Reaction rate as a function of total mass; the unit-slope dashed green line corresponds to linear kinetics.

328 4.2. Weak-coupling approximation

329 As formalized in Eqs. (24) and (25), determining the dynamics of the total
 330 mass of reactant $M(t)$ reduces to computing the temporal evolution of the
 331 position of the regime interface $\xi(t)$ between the linear and saturated regimes,
 332 along with the diffusive flux $f(t)$ thereat. To solve this problem, it is sufficient
 333 to develop an approximation for the concentration distribution in the saturated
 334 regime $c_s(x, t)$, because the reaction dynamics in the linear regime are indepen-
 335 dent of the concentration profile.

336 In the saturated regime, the local reaction rate $r(c)$ is constant and equal to

337 α , and the corresponding reactive transport equation is

$$\partial_t c_s = \frac{\partial_x^2 c_s}{2\text{Da}} - \alpha. \quad (29)$$

338 Defining, for $|x| < \xi(t)$, $c_D = c_s + \alpha t$, c_D solves the conservative equation

$$\partial_t c_D = \frac{\partial_x^2 c_D}{2\text{Da}}. \quad (30)$$

339 Solving this equation is not trivial in general, since it depends on the boundary
 340 condition at the interface $x = \pm\xi(t)$ with the linear regime. Neglecting the effect
 341 of the boundary condition on the shape of the saturated part of the profile, we
 342 obtain, for $|x| < \xi(t)$, the solution

$$c_D(x, t) \approx \sqrt{\frac{\text{Da}}{2\pi(\text{Da} + t)}} e^{-\frac{\text{Da} x^2}{2(\text{Da} + t)}}, \quad (31)$$

343 and

$$c_s(x, t) = [c_D(x, t) - \alpha t]H[\xi(t) - |x|]. \quad (32)$$

344 Thus, assuming that the linear regime does not significantly influence the
 345 shape of the profile in the saturated regime leads to a weak-coupling approx-
 346 imation for the dynamics of diffusion and reaction: the concentration in the
 347 saturated regime is the result of superimposing a linear concentration decay
 348 $-\alpha t$ corresponding to the constant rate $r(c) = \alpha$ on the conservative diffusion
 349 problem. This leads, for the interface behavior, to

$$\xi(t) \approx \sqrt{\frac{\text{Da} + t}{\text{Da}}} \ln \left[\frac{\text{Da}}{2\pi\alpha^2(1+t)^2(\text{Da} + t)} \right], \quad (33a)$$

$$f(t) \approx \alpha\xi(t) \frac{1+t}{\text{Da} + t}, \quad (33b)$$

350 valid for $t \leq \sigma$, the duration of the saturated regime. For $t \geq \sigma$, we set
 351 $\xi(t) = f(t) = 0$ as discussed before.

352 As mentioned above, we consider configurations for which the saturated
 353 regime is present initially, which means that the maximum initial concentration
 354 is above α . For the Gaussian initial condition, this means $\alpha < \sqrt{2\pi}$. Time
 355 σ then corresponds to the time when the peak of the concentration profile, at

356 $x = 0$, reaches α . It follows that σ solves $\xi(\sigma) = 0$, which gives

$$(1 + \sigma)^2(\text{Da} + \sigma) \approx \frac{\text{Da}}{2\pi\alpha^2}. \quad (34)$$

357 This is a cubic equation for σ with a single positive root. An analytical solution
358 exists, but it is not particularly useful or insightful, and the root can easily be
359 found numerically.

360 Under the weak coupling approximation, the saturated-regime mass has the
361 analytical solution

$$M_s(t) = \text{erf} \left[\sqrt{\frac{\text{Da}}{\text{Da} + t}} \frac{\xi(t)}{\sqrt{2}} \right] - 2\alpha t \xi(t). \quad (35)$$

362 While we are not aware of a general closed-form solution for the mass in the lin-
363 ear regime, the latter can easily be obtained by numerically computing the inte-
364 grals in Eq. (24b). The total mass is then the sum of the two regime masses, and
365 the effective kinetics r_M can be computed from Eq. (18). In the diffusion- and
366 reaction-dominated limits, analytical solutions can be obtained; these regimes
367 are discussed in detail in [Appendix C](#).

368 4.3. Effective kinetics

369 We compare the results for the total mass and the temporal effective kinet-
370 ics $r_t(t)$ under the weak coupling approximation against numerical simulations
371 in Fig. 7. Overall, the approximation provides very good predictions. Unsur-
372 prisingly, $\text{Da} \sim 1$ together with low values of α leads to the most discrepancy
373 between simulations and semi-analytical solutions, since it corresponds to a
374 long saturated regime with reaction and diffusion acting on similar timescales.
375 Nonetheless, the weakly-coupled formulation provides a reasonable approxima-
376 tion even in this regime, capturing the main features of the dynamics of the
377 total mass. A more detailed analysis of the performance of this approximation
378 in terms of the interface dynamics is provided in [Appendix D](#).

379 We now use the weak-coupling approximation to gain insight into the en-
380 hancement and non-monotonic behavior of the effective kinetics. The latter can

381 be understood by examining the derivative dr_M/dm . In particular, the condi-
 382 tion for non-monotonic effective kinetics is $dr_M(m=1)/dm < 0$, because the
 383 linear regime is always reached for small masses m , so that $dr_M(m)/dm = 1 > 0$.
 384 Using the chain rule in Eq. (18) for the effective mass kinetics, we obtain for
 385 the change in reaction rate with total mass

$$\frac{dr_M(m)}{dm} = \frac{\dot{M}[T(m)]}{r_M(m)}. \quad (36)$$

386 As shown in [Appendix E](#), the first and second times derivatives of the total
 387 mass are given by

$$\dot{M}(t) = -M_\ell(t) - 2\alpha\xi(t), \quad (37a)$$

$$\ddot{M}(t) = M_\ell(t) - f(t). \quad (37b)$$

388 The interpretation of the first result is straightforward: The total rate of loss of
 389 mass is the sum of the reactive mass loss rates in each regime, with the linear
 390 regime being characterized by a rate proportional to mass, and the saturated
 391 regime consuming concentration at a constant rate α within a region of length
 392 2ξ . The remaining terms involved in the change of the mass in each regime
 393 correspond to transfer between regimes and therefore do not affect the total
 394 mass. The result for the temporal change \ddot{M} in the rate \dot{M} of mass consumption
 395 is more subtle, because it is affected by transfer processes. The rate in the linear
 396 regime changes according to the negative of the change of mass therein due to
 397 the linear character of the reaction. In the saturated regime, the reaction rate
 398 changes as $2\alpha\dot{\xi}$ due to change in size of the saturated region; thus, the rate of
 399 change of mass, which is the negative of the reaction rate, changes as $-2\alpha\dot{\xi}$. In
 400 turn, the mass in the linear regime changes as $-2\alpha\dot{\xi}$ due to movement of the
 401 boundary, compensating the change in saturated-regime rate. Finally, the mass
 402 in the linear regime also increases according to the diffusive flux $f(t)$. The net
 403 rate change resulting from these processes is given by $M_\ell(t) - f(t)$.

404 The result for $\dot{M}(t)$ leads, according Eq. (18), to

$$r_M(m) = M_\ell[T(m)] + 2\alpha\xi[T(m)], \quad (38)$$

405 and, using the result for $\ddot{M}(t)$, we find

$$\frac{dr_M(m)}{dm} = \frac{M_\ell[T(m)] - f[T(m)]}{M_\ell[T(m)] + 2\alpha\xi[T(m)]}. \quad (39)$$

406 The initial condition, corresponding to unit mass $m = 1$ and time $T(m = 1) = 0$,
407 is characterized by

$$\left. \frac{dr_M(m)}{dm} \right|_{m=1} = \frac{M_\ell(0) - f(0)}{M_\ell(0) + 2\alpha\xi(0)}. \quad (40)$$

408 Thus, if $M_\ell(0) \geq f(0)$, the initial change in the reaction rate is nonnegative,
409 and the maximum reaction rate occurs for $m = 1$ ($t = 0$). For $M_\ell(0) < f(0)$,
410 the effective kinetics are non-monotonic and the maximum reaction rate occurs
411 at some intermediate value $m_c = M_\ell(t_c) = f(t_c)$, corresponding to some time
412 $0 < t_c \leq \sigma$.

413 We will now identify three qualitative Damköhler number regimes of reaction
414 enhancement. These are characterized by two transition Damköhler numbers,
415 Da_1 and Da_2 , such that the three regimes correspond to $Da \leq Da_1$, $Da_1 < Da <$
416 Da_2 , and $Da \geq Da_2$. We consider first the upper transition number Da_2 . Using
417 Eqs. (27), (28), and (33b) for the initial masses, interface position, and boundary
418 flux under the weak-coupling approximation, the condition $M_\ell(0) < f(0)$ for
419 dr_M/dm to switch signs at some intermediate mass m_c becomes $Da < Da_2$,
420 where

$$Da_2 = \frac{\alpha\sqrt{-\ln(2\pi\alpha^2)}}{\operatorname{erfc}[\sqrt{-\ln(2\pi\alpha^2)}/2]}. \quad (41)$$

421 We note that this criterion is well approximated by the small- and large- α
422 expansions

$$Da_2 \approx \begin{cases} -\ln(\sqrt{2\pi\alpha^2}), & \alpha \ll 1 \\ \sqrt{\frac{1-\sqrt{2\pi\alpha^2}}{\pi}}, & 1 - \sqrt{2\pi\alpha^2} \ll 1 \end{cases}, \quad (42)$$

423 with the crossover between these two α -dependencies occurring for $\alpha \approx 0.2$.

424 For a given α and $Da \geq Da_2$, the effective kinetics are monotonic and the
425 maximum rate occurs at $m = 1$. It is given by $r_M(1) = M_I(0) + 2\alpha\xi(0)$ (from
426 Eq. (38)). Using Eqs. (27) and (28), we obtain for the maximum enhancement,

$$427 \quad \tilde{r}_{\max} = r_{\max}/\alpha,$$

$$\tilde{r}_{\max} = \alpha^{-1} \operatorname{erfc} \left[\sqrt{-\ln(2\pi\alpha^2)}/2 \right] + 2\sqrt{-\ln(2\pi\alpha^2)}. \quad (43)$$

428 Note the independence on Da. This expression is well approximated by the low-
429 and high- α expansions

$$\tilde{r}_{\max} \approx \begin{cases} 2 \frac{1-\ln(2\pi\alpha^2)}{\sqrt{-\ln(2\pi\alpha^2)}}, & \alpha \ll 1 \\ \sqrt{2\pi} \left[1 + (1 - \sqrt{2\pi\alpha^2}) \right], & 1 - \sqrt{2\pi\alpha^2} \ll 1 \end{cases}, \quad (44)$$

430 with the crossover occurring for $\alpha \approx 0.1$.

431 Next, we consider the limit of small Da for a given α . For sufficiently
432 small Da, we have $\text{Da} < \text{Da}_2$, so that the effective kinetics are non-monotonic.
433 Diffusion-dominated dynamics occur for $\text{Da} \ll \pi\alpha^2$, see Eq. (Appendix C.23)
434 in Appendix C.2. In this regime, we have $M_\ell(t) \approx 1$ for $t \leq \sigma$. Us-
435 ing Eqs. (Appendix C.20) and (Appendix C.22) for the boundary position
436 and flux under diffusion-dominated dynamics, we obtain $t_c \approx \sigma_D$, see also
437 Eq. (Appendix C.21). We conclude that $r_{\max} \approx M_\ell(\sigma) \approx 1$. This means
438 that, in agreement with the trend observed in Fig. 6c, in the limit of small Da
439 at fixed α the maximum reaction rate is approximately unity and occurs after
440 diffusion has placed roughly all the mass in the linear regime, with little loss
441 due to reaction. Thus, in this limit, the maximum reaction enhancement is

$$\tilde{r}_{\max} = 1/\alpha, \quad (45)$$

442 independent of Da to leading order. Since this regime occurs for $\text{Da} \ll \pi\alpha^2$, we
443 set

$$\text{Da}_1 = \pi\alpha^2/10, \quad (46)$$

444 so that the regime is characterized by $\text{Da} \lesssim \text{Da}_1$.

445 For a given α , the dependence of the maximum effective reaction rate on Da
446 thus follows three regimes: (i) a plateau of maximum enhancement for low Da
447 below a first transition Damköhler Da_1 ; (ii) a decrease of the maximum reac-
448 tion rate up to a second transition Damköhler Da_2 ; and (iii) a second plateau

449 at large Damköhler. The weak coupling approximation accurately captures the
 450 non-monotonic behavior of the effective kinetics (Fig. 8a) and their enhance-
 451 ment relative to the batch kinetics (Fig. 8b). The weak coupling approximation
 452 allows for deriving analytical expressions for the two plateaus and the associated
 453 transition Damköhler numbers, and for accurate and efficient numerical compu-
 454 tation of the complex intermediate-Da behavior. We summarize these findings
 455 in Fig. 9.

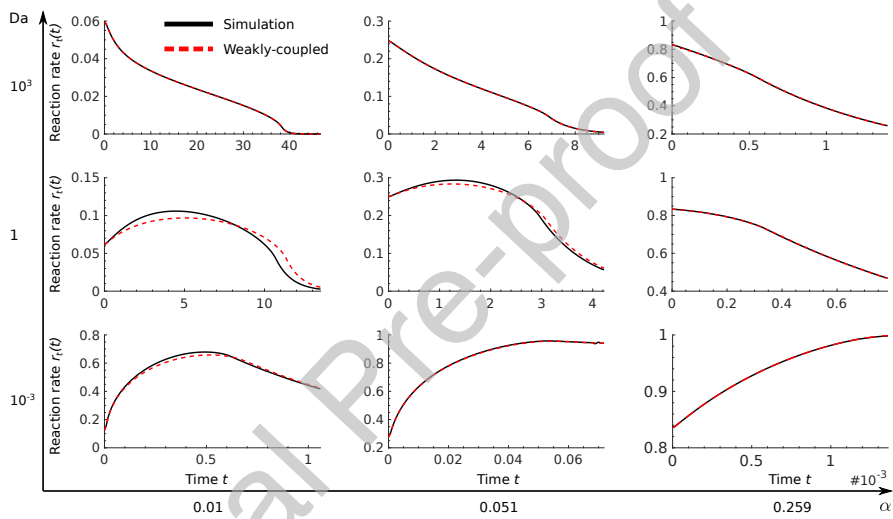


Figure 7: Temporal evolution of the effective reaction rate for a Gaussian initial condition, computed from simulations (black) and based on the weak-coupling approximation (dashed red).

456 5. Accelerated consumption of nutrient pulses by bacteria

457 To illustrate the phenomena described above, we compute effective reaction
 458 rates for nutrient pulses consumed by bacteria under Michaelis–Menten kinetics
 459 and investigate the influence of pulse size on the maximum reaction rate. We
 460 consider Michaelis–Menten parameters representative of nutrient consumption
 461 by *E. coli* [44], see Eq. (1) and Table 1.

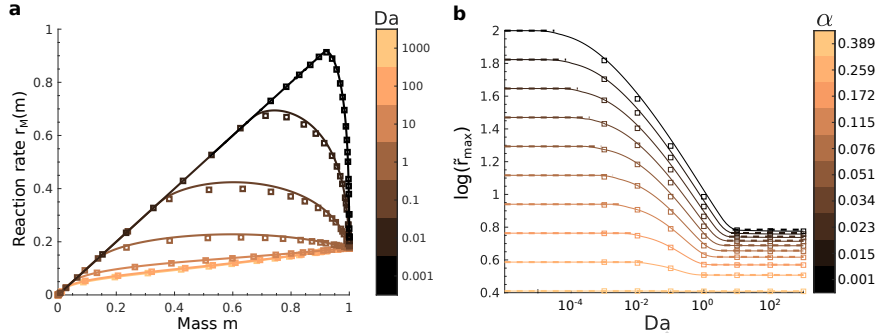


Figure 8: Performance of the weak-coupling approximation in describing the effective reaction kinetics as a function of total mass, for a Gaussian initial condition. The weakly-coupled model predictions are shown as solid lines and the results of numerical simulations as squares. **(a)** Effective reaction rate as a function of mass for maximum batch rate $\alpha = 0.05$ and varying Damköhler number Da . **(b)** Maximum reaction rate as a function of Damköhler number Da for different α ; the dashed lines show the analytical predictions for the high- and low- Da plateaus, occurring respectively for $Da \leq Da_1$ and $Da \geq Da_2$.

462 We consider a pulse of nutrient in a solution of homogeneous bacterial con-
 463 centration B . We assume here that the bacterial concentration does not evolve
 464 in time, which requires the division rate to be much slower than the nutrient
 465 consumption rate. The nutrient is introduced as a pulse of width s_0 in the di-
 466 rection x and uniform in the y and z directions. In the x direction, the spatial
 467 domain is assumed much wider than the pulse at all times, and in the y - z plane
 468 the latter is assumed to occupy the full available area S . While we focus here
 469 on the one-dimensional problem, the derivations above could easily be extended
 470 to localized pulses in three-dimensional systems by expressing Eq. (13) in radial
 471 coordinates. The nutrient pulse thus diffuses in the x direction and follows the
 472 reactive transport equation (13), where the maximum consumption rate μ is a
 473 function of the concentration B of bacteria,

$$\mu = \mu_c B, \quad (47)$$

474 with μ_c the rate of consumption of the nutrient by a single bacterium. For a
 475 given initial (dimensional) mass M'_0 of nutrient, the initial nutrient concentra-

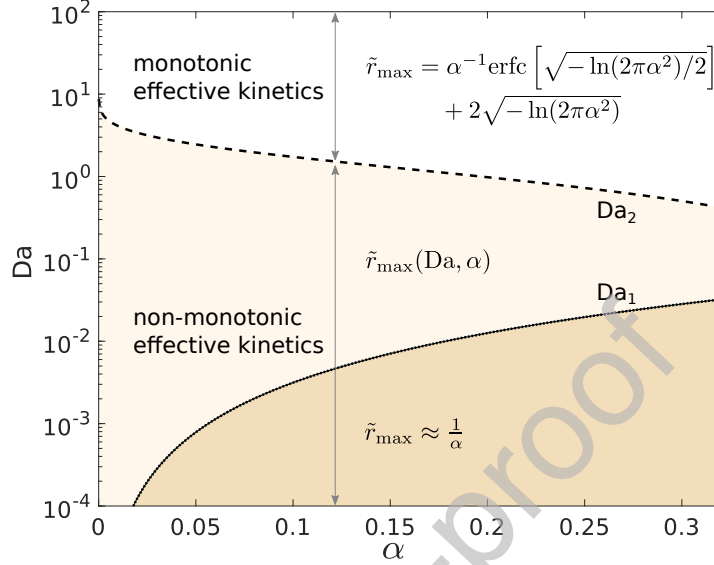


Figure 9: Regimes of effective kinetics in the α - Da space for a Gaussian initial pulse. The dotted line shows the first transition Damköhler number Da_1 , which marks the upper limit of the maximum-enhancement regime. The dashed line shows the second transition Damköhler number Da_2 , which determines the onset of the second (lowest) reaction enhancement plateau associated with monotonic effective kinetics. Analytical solutions for \tilde{r}_{max} in the end-member regimes below Da_1 and above Da_2 are indicated.

476 tion is $c'_0 = M'_0/(s_0S)$. Therefore, α is given by

$$\alpha = s_0KS/M'_0, \quad (48)$$

477 covering a broad range of values depending on pulse size.

478 Figure 10a shows the Damköhler number associated with a given pulse width
 479 s_0 and bacterial concentration B , expressed as a fraction of the maximum bac-
 480 terial concentration B_{max} [45]. Since the Damköhler number is proportional to
 481 $s_0^2\mu$, see Eq. (12), it varies broadly with pulse size and bacterial concentration.
 482 Expressing s_0 in terms of α , the system's trajectory in the Da - α plane when
 483 varying s_0 is therefore characterized by the relation

$$Da = \frac{M_0'^2\mu}{2DK^3S^2}\alpha^2. \quad (49)$$

484 We show these trajectories for different bacterial concentrations in Fig. 10b.
485 When varying the initial pulse size of a pulse of given mass, all the different
486 regimes discussed in the previous sections are explored, from low Da and α for
487 small pulses, which corresponds to the maximum enhancement relative to the
488 batch, to large Da and α , which corresponds to the reaction-dominated regime,
489 where the global and local kinetics are identical. For large s_0 , and therefore
490 low c_0 , most of the mass is initially in the linear regime. In this situation, the
491 effective reaction rate is therefore maximum. Similar reaction rates are however
492 reached in the opposite situation of sharp and highly concentrated pulses due
493 to the effects discussed above. The system thus exhibits two optima at low
494 and high s_0 . The lowest effective reaction rate is reached for intermediate pulse
495 sizes (blue area in Fig. 10b), where a large portion of the mass remains in the
496 saturated regime for a long time.

497 For this simple, yet very common, scenario of a nutrient pulse consumed by
498 bacteria, these results illustrate some of the non-trivial consequences of our find-
499 ings. For different pulse sizes, a broad range of the Da - α space is explored where
500 the different regimes uncovered in our analysis occur. Our results could there-
501 fore provide a guide for understanding natural systems or designing bacterial
502 cultures under non-uniform nutrient conditions. In practice, these phenomena
503 should be expected to be coupled to other important processes such as bacterial
504 growth, chemotaxis, or biofilm development, which further increase the system's
505 complexity.

Table 1: Parameters used to investigate the effective kinetics of nutrient pulses under consumption by bacteria, relating to *E. coli* [44]. Values are representative of glucose consumption.

Parameter	Value	Unit
D	10^{-9}	$\text{m}^2.\text{s}^{-1}$
s_0	$10^{-5}-10^{-1}$	m
M'_0	10^{-6}	kg
μ_c	5.10^{-20}	$\text{kg}.\text{cell}^{-1}.\text{s}^{-1}$
B_{\max}	10^{15}	$\text{cell}.\text{m}^{-3}$
S	10^{-2}	m^2

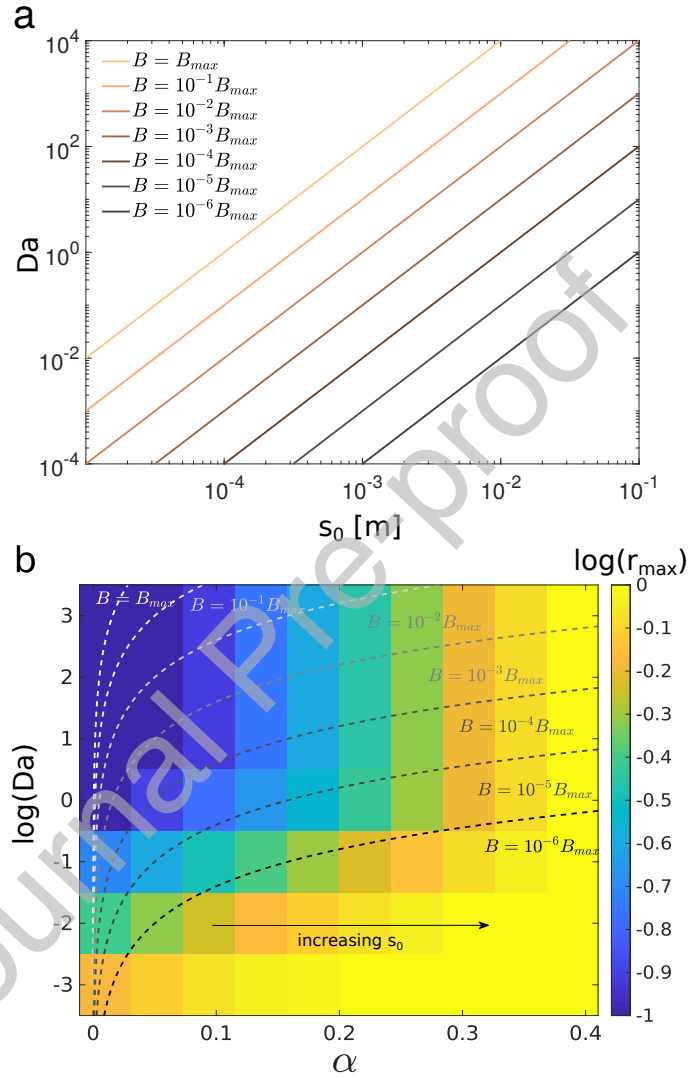


Figure 10: (a) Damköhler number Da as a function of pulse size s_0 for different bacterial concentrations. (b) Trajectories in the Da - α plane corresponding to varying the pulse size s_0 from $10 \mu\text{m}$ to 10cm for a given nutrient mass. Solid lines correspond to different bacterial concentrations B , superimposed on the corresponding maximum effective reaction rate r_{max} .

506 6. Conclusions

507 We have investigated the kinetics of solute pulses locally subject to a Michaelis-
508 Menten reaction, which occur in many natural and industrial systems. We have
509 analyzed the effective (i.e., global) kinetics of such pulse reactors by represent-
510 ing the rate of mass change as a function of mass. While for linear local kinetics
511 the global effective kinetics are also linear, under nonlinear kinetics the global
512 behavior differs from the local kinetics. In the present problem, the nonlinearity
513 arises from the transition from linear to constant local reaction rate due to sat-
514 uration. Spatial heterogeneity in the concentration profile causes the transition
515 to occur at different times for different spatial locations. This fact underlies the
516 difference between local and global kinetics.

517 The coupling of diffusion and nonlinear kinetics can lead to non-monotonic
518 effective kinetics, characterized by an initial enhancement of the effective reac-
519 tion rate up to a maximum, followed by a linear decay of the reaction rate. This
520 enhancement is mediated by diffusion, which transfers mass from regions where
521 the kinetics are saturated to others where it is linear, i.e., where the reaction
522 rate is locally proportional to concentration. This mechanism can significantly
523 accelerate the effective kinetics of pulse reactors relative to a batch reactor of
524 the same size as the initial pulse, in which reactants are spatially homogeneous.
525 The precise kinetics depend on the initial condition, as illustrated by comparing
526 the square initial pulse (Fig. 3) to the Gaussian initial pulse (Fig. 6) but the en-
527 hancement of effective kinetics through the coupling of diffusion and reaction is
528 expected to be a general result. For any non-uniform initial condition, diffusion
529 always accelerates the transfer of mass from the saturated regime to the linear
530 kinetics regime, leading to faster average kinetics than in batch conditions.

531 We have numerically explored the different regimes that emerge from this
532 nonlinear reactive transport problem, and shown that they can be adequately
533 understood and quantified using a weak-coupling approximation. This approxi-
534 mation leads to analytical expressions that predict the transitions between differ-
535 ent regimes and quantify the enhancement of reaction rates in the end-member

536 scenarios. We have considered here a piecewise-linear approximation of the
537 Michaelis-Menten kinetics to facilitate analytical derivations. Our methodology
538 could be extended to more complex analytical solutions of full Michaelis-Menten
539 kinetics [21, 20] for a more precise analysis of reaction enhancement close to the
540 transition between first-order and zero-order kinetics. The mechanisms of reac-
541 tion enhancement discussed here for one-dimensional diffusion are qualitatively
542 similar as those occurring in three dimensions as discussed in [Appendix G](#) and
543 analytical solutions in spherical coordinates can be derived following the same
544 approach. Since the diffusion-reaction equation is the same of the diffusion-
545 reaction equation studied here, the mechanisms described here are also relevant
546 for conventional dispersion processes. The effect of more complex mixing pat-
547 terns induced by shear and stretching [46] could be investigated using a similar
548 approach by considering stretching enhanced diffusion captured by lamella mix-
549 ing models [47].

550 We have illustrated the consequences of these findings by investigating the
551 dynamics of consumption of nutrient pulses by bacteria. Varying the bacterial
552 concentration and pulse size allows for exploring the different regimes of non-
553 linear effective kinetics. For a given mass of nutrient, the consumption kinetics
554 are characterized by two maxima, respectively for localized, highly concentrated
555 pulses and for wide, dilute pulses. A minimum consumption rate is obtained
556 for intermediate pulse sizes and concentrations. These findings provide new
557 clues to understand natural bio-reactive systems and potentially optimize en-
558 gineered bacterial cultures, either to maximize or minimize consumption rates
559 under non-uniform nutrient landscapes. Furthermore, these results provide a
560 new framework to understand and model the effective kinetics of Michaelis-
561 Menten reactions in non-homogeneous concentration fields. While these kinetics
562 are well known in batch reactors, we have uncovered a rich array of behaviors
563 that arise from the coupling of concentration gradients and nonlinear kinetics.
564 These results are relevant to a broad range of reactive systems characterized by
565 saturating kinetics and non-uniform concentration landscapes.

566 **Data statement**

567 The code used for simulations we will provided upon requests.

568 **Declaration of Competing Interest**

569 The authors declare no competing interest.

570 **Acknowledgments**

571 AH, HT, YM and TLB gratefully acknowledge funding by the ERC under
572 the project *ReactiveFronts* 648377. TA is supported by a Marie Skłodowska
573 Curie Individual Fellowship, under the project *ChemicalWalks* 792041.

574 **References**

575 **References**

- 576 [1] L. Michaelis, M. L. Menten, The kinetics of the inversion effect, *Biochem.*
577 *Z* 49 (1913) 333–369.
- 578 [2] L. A. Segel, M. Slemrod, The quasi-steady-state assumption: a case study
579 in perturbation, *SIAM review* 31 (3) (1989) 446–477.
- 580 [3] A. Holmberg, On the practical identifiability of microbial growth models
581 incorporating Michaelis–Menten type nonlinearities, *Math. Biosci.* 62 (1)
582 (1982) 23–43.
- 583 [4] M. Thullner, P. Regnier, Microbial controls on the biogeochemical dynamics
584 in the subsurface, *Reviews in Mineralogy and Geochemistry* 85 (1) (2019)
585 265–302.
- 586 [5] A. Novick-Cohen, L. Segel, A gradually slowing travelling band of chemo-
587 tactic bacteria, *Journal of mathematical biology* 19 (1) (1984) 125–132.

- 588 [6] J. P. Ward, J. R. King, Mathematical modelling of drug transport in tu-
589 mour multicell spheroids and monolayer cultures, *Mathematical biosciences*
590 181 (2) (2003) 177–207.
- 591 [7] P. Hiltmann, P. Lory, On oxygen diffusion in a spherical cell with michaelis-
592 menten oxygen uptake kinetics, *Bulletin of Mathematical Biology* 45 (5)
593 (1983) 661–664.
- 594 [8] D. McElwain, A re-examination of oxygen diffusion in a spherical cell with
595 michaelis-menten oxygen uptake kinetics, *Journal of Theoretical Biology*
596 71 (2) (1978) 255–263.
- 597 [9] C. Nicholson, Interaction between diffusion and michaelis-menten uptake of
598 dopamine after iontophoresis in striatum, *Biophysical journal* 68 (5) (1995)
599 1699–1715.
- 600 [10] C. Horvath, J.-M. Engasser, External and internal diffusion in heteroge-
601 neous enzymes systems, *Biotechnology and Bioengineering* 16 (7) (1974)
602 909–923.
- 603 [11] S.-B. Hsu, T.-W. Hwang, Y. Kuang, Global analysis of the Michaelis-
604 Menten-type ratio-dependent predator-prey system, *J of Math. Biol.* 42 (6)
605 (2001) 489–506.
- 606 [12] E. Michael, et al., Reaction/diffusion with michaelis-menten kinetics in
607 electroactive polymer films. part 1. the steady-state amperometric response,
608 *Analyst* 121 (6) (1996) 715–731.
- 609 [13] J. Monod, The growth of bacterial cultures, *Annual review of microbiology*
610 3 (1) (1949) 371–394.
- 611 [14] A. Tompson, R. Knapp, M. Hanna, R. Taylor, Simulation of tce migration
612 and biodegradation in a porous medium under conditions of finite degra-
613 dation capacity, *Advances in water resources* 17 (4) (1994) 241–249.

- 614 [15] G. Porta, D. la Cecilia, A. Guadagnini, F. Maggi, Implications of uncertain
615 bioreactive parameters on a complex reaction network of atrazine biodegra-
616 dation in soil, *Advances in water resources* 121 (2018) 263–276.
- 617 [16] D. Barry, H. Prommer, C. Miller, P. Engesgaard, A. Brun, C. Zheng, Mod-
618 elling the fate of oxidisable organic contaminants in groundwater, *Advances*
619 *in Water Resources* 25 (8-12) (2002) 945–983.
- 620 [17] J. S. Kindred, M. A. Celia, Contaminant transport and biodegradation: 2.
621 conceptual model and test simulations, *Water Resources Research* 25 (6)
622 (1989) 1149–1159.
- 623 [18] P. Blum, D. Hunkeler, M. Weede, C. Beyer, P. Grathwohl, B. Morasch,
624 Quantification of biodegradation for *o*-xylene and naphthalene using first
625 order decay models, michaelis–menten kinetics and stable carbon isotopes,
626 *Journal of contaminant hydrology* 105 (3-4) (2009) 118–130.
- 627 [19] T. Ginn, C. Simmons, B. Wood, Stochastic-convective transport with non-
628 linear reaction: Biodegradation with microbial growth, *Water Resources*
629 *Research* 31 (11) (1995) 2689–2700.
- 630 [20] S. Schnell, C. Mendoza, Closed form solution for time-dependent enzyme
631 kinetics, *Journal of theoretical Biology* 187 (2) (1997) 207–212.
- 632 [21] F. Maggi, D. la Cecilia, Implicit analytic solution of michaelis–menten–
633 monod kinetics, *ACS omega* 1 (5) (2016) 894–898.
- 634 [22] D. Shanthi, V. Ananthaswamy, L. Rajendran, Analysis of non-linear
635 reaction-diffusion processes with michaelis-menten kinetics by a new ho-
636 motopy perturbation method.
- 637 [23] S.-B. Hsu, P. Waltman, On a system of reaction-diffusion equations arising
638 from competition in an unstirred chemostat, *SIAM Journal on Applied*
639 *Mathematics* 53 (4) (1993) 1026–1044.

- 640 [24] N. Anderson, A. Arthurs, Analytical bounding functions for diffusion prob-
641 lems with michaelis-menten kinetics, *Bulletin of Mathematical Biology*
642 47 (1) (1985) 145–153.
- 643 [25] N. Anderson, A. M. Arthurs, Complementary variational principles for dif-
644 fusion problems with michaelis-menten kinetics, *Bulletin of Mathematical*
645 *Biology* 42 (1) (1980) 131–135.
- 646 [26] S. Park, N. Agmon, Theory and simulation of diffusion-controlled michaelis-
647 menten kinetics for a static enzyme in solution, *The Journal of Physical*
648 *Chemistry B* 112 (19) (2008) 5977–5987.
- 649 [27] I. Battiato, D. Tartakovsky, Applicability regimes for macroscopic models
650 of reactive transport in porous media, *Journal of contaminant hydrology*
651 120 (2011) 18–26.
- 652 [28] I. Battiato, D. M. Tartakovsky, A. M. Tartakovsky, T. Scheibe, On break-
653 down of macroscopic models of mixing-controlled heterogeneous reactions
654 in porous media, *Advances in water resources* 32 (11) (2009) 1664–1673.
- 655 [29] C. Meile, K. Tuncay, Scale dependence of reaction rates in porous media,
656 *Advances in Water Resources* 29 (1) (2006) 62–71.
- 657 [30] J. Guo, M. Quintard, F. Laouafa, Dispersion in porous media with het-
658 erogeneous nonlinear reactions, *Transport in Porous Media* 109 (3) (2015)
659 541–570.
- 660 [31] F. Heße, F. A. Radu, M. Thullner, S. Attinger, Upscaling of the advection–
661 diffusion–reaction equation with monod reaction, *Advances in water re-*
662 *sources* 32 (8) (2009) 1336–1351.
- 663 [32] B. D. Wood, K. Radakovich, F. Golfier, Effective reaction at a fluid–solid
664 interface: Applications to biotransformation in porous media, *Advances in*
665 *water resources* 30 (6-7) (2007) 1630–1647.

- 666 [33] F. Hesse, H. Harms, S. Attinger, M. Thullner, Linear exchange model for
667 the description of mass transfer limited bioavailability at the pore scale,
668 *Environmental Science & Technology* 44 (6) (2010) 2064–2071, PMID:
669 20175545.
- 670 [34] S. I. Schmidt, J.-U. Kreft, R. Mackay, C. Picioreanu, M. Thullner, Elu-
671 cidating the impact of micro-scale heterogeneous bacterial distribution on
672 biodegradation, *Advances in water resources* 116 (2018) 67–76.
- 673 [35] G. Sole-Mari, D. Fernández-García, P. Rodríguez-Escales, X. Sanchez-Vila,
674 A kde-based random walk method for modeling reactive transport with
675 complex kinetics in porous media, *Water resources research* 53 (11) (2017)
676 9019–9039.
- 677 [36] D. Ding, D. A. Benson, Simulating biodegradation under mixing-limited
678 conditions using michaelis-menten (monod) kinetic expressions in a particle
679 tracking model, *Advances in water resources* 76 (2015) 109–119.
- 680 [37] S. König, A. Worrlich, T. Banitz, F. Centler, H. Harms, M. Kästner, A. Milt-
681 ner, L. Y. Wick, M. Thullner, K. Frank, Spatiotemporal disturbance char-
682 acteristics determine functional stability and collapse risk of simulated mi-
683 crobial ecosystems, *Scientific reports* 8 (1) (2018) 1–13.
- 684 [38] B. G. Waring, J. S. Powers, Unraveling the mechanisms underlying pulse
685 dynamics of soil respiration in tropical dry forests, *Environmental Research*
686 *Letters* 11 (10) (2016) 105005.
- 687 [39] D. M. Orcutt, E. T. Nilsen, *Physiology of plants under stress: Soil and*
688 *biotic factors*, Vol. 2, John Wiley & Sons, 2000.
- 689 [40] O. Bochet, L. Bethencourt, A. Dufresne, J. Farasin, M. Pédrot,
690 T. Labasque, E. Chatton, N. Lavenant, C. Petton, B. W. Abbott, et al.,
691 Iron-oxidizer hotspots formed by intermittent oxic–anoxic fluid mixing in
692 fractured rocks, *Nature Geoscience* (2020) 1–7.

- 693 [41] G. Weigelhofer, J. P. Ramião, A. Puritscher, T. Hein, How do chronic
694 nutrient loading and the duration of nutrient pulses affect nutrient uptake
695 in headwater streams?, *Biogeochemistry* 141 (2) (2018) 249–263.
- 696 [42] J. W. Haefner, *Modeling Biological Systems:: Principles and Applications*,
697 Springer Science & Business Media, 2005.
- 698 [43] M. Dentz, T. Le Borgne, A. Englert, B. Bijeljic, Mixing, spreading and
699 reaction in heterogeneous media: A brief review, *Journal of contaminant*
700 *hydrology* 120 (2011) 1–17.
- 701 [44] A. Natarajan, F. Sreenc, Glucose uptake rates of single e. coli cells grown
702 in glucose-limited chemostat cultures, *Journal of microbiological methods*
703 42 (1) (2000) 87–96.
- 704 [45] A. L. Koch, Some calculations on the turbidity of mitochondria and bac-
705 teria, *Biochimica et biophysica acta* 51 (3) (1961) 429–441.
- 706 [46] M. Rolle, T. Le Borgne, Mixing and reactive fronts in the subsurface, *Re-*
707 *views in Mineralogy and Geochemistry* 85 (1) (2019) 111–142.
- 708 [47] T. Le Borgne, M. Dentz, E. Villermaux, The lamellar description of mixing
709 in porous media, *Journal of Fluid Mechanics* 770 (2015) 458498.

710 **Appendix A. Sensitivity of the effective kinetics on Da and α**

711 In this appendix, we provide additional numerical results illustrating how the
712 effective kinetics depend on Da and α . The non-monotonic nature of the effective
713 kinetics is enhanced for decreasing Da and increasing α (Fig. A.11). For low
714 Da (Fig. A.11a), the maximum reaction rate initially increases markedly with
715 decreasing mass before converging to linear decay. For high Da (Fig. A.11c), the
716 effective kinetics approach the local kinetics. For increasing α at fixed Da , the
717 maximum reaction rate increases and occurs for higher masses (Fig. A.11d-f).

718 At late times, once the peak concentration drops below α , both the pulse
719 and batch kinetics are linear. The transition to linear kinetics happens at time

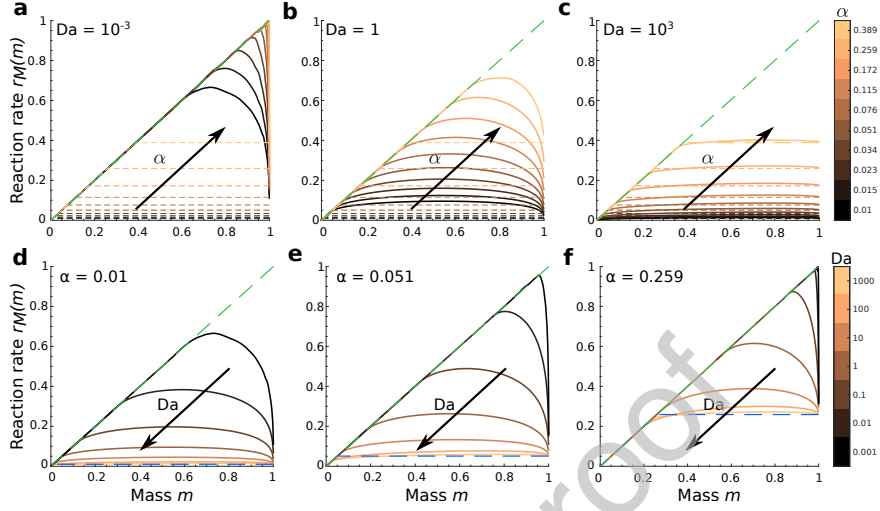


Figure A.11: Reaction rate as a function of total mass. Batch kinetics are shown as dashed lines for each value of the maximum batch rate α . Linear kinetics are indicated by dashed green lines with unit slope. The top row shows the behavior for different values of α at three fixed Damköhler number Da values. Conversely, the bottom row shows the behavior for varying Da at three fixed α values, with the corresponding batch kinetics represented by a dashed blue line.

720 σ for the diffusive problem and σ_B for the batch problem. When all the mass
 721 is in the linear regime, mass and reaction rates decay exponentially at unit rate
 722 regardless of the mixing state, see Eqs. (15) and (16). Thus, $\tilde{r}(t)$ is constant at
 723 times larger than both σ_B and σ and given by the ratio of surviving masses,

$$\lambda = \tilde{r}(t) = \frac{M(t)}{M_B(t)}, \quad t \geq \max\{\sigma_B, \sigma\}. \quad (\text{Appendix A.1})$$

724 As σ is always smaller than σ_B , the value of λ can be obtained by evaluating the
 725 mass ratio for any time $t \geq \sigma_B$. Taking $t = \sigma_B$ and using Eqs. (10) and (15),
 726 we find

$$\lambda = \frac{M(\sigma)}{\alpha} e^{-(\sigma_B - \sigma)}, \quad (\text{Appendix A.2})$$

727 and $\eta = 1 - \lambda$ is thus a measure of the overall enhancement of the effective
 728 reaction rate. The larger η , the more efficient the diffusing-pulse reactor is
 729 when compared to the batch reactor, with $\eta = 1$ ($\lambda = 0$) being the largest

730 possible value. A value of $\eta = 0$ ($\lambda = 1$) means that mixing has no effect
 731 on the overall reaction efficiency. Negative values of η would mean that the
 732 incompletely-mixed system is less efficient than the batch, but these do not
 733 occur for Michaelis–Menten reactions.

734 We show the dependence of the overall reaction enhancement η on Da and
 735 α in Fig. A.12. When α is low, both the diffusion and batch problems start
 736 from highly-saturated conditions. These conditions correspond to less-efficient
 737 overall reaction when compared to linear kinetics, since the effective kinetics are
 738 constant rather than linearly increasing with total mass. In the batch problem,
 739 exiting the saturated regime requires mass to be consumed until the uniform
 740 concentration drops below α , which means reaction proceeds under saturated
 741 conditions for a long time. On the other hand, when Da is low, diffusion can
 742 quickly deform the concentration profile so that a significant portion of mass
 743 reacts under linear conditions, leading to substantially increased overall reac-
 744 tion efficiency. Increasing α corresponds to less-saturated initial conditions; the
 745 duration of the saturated regime is reduced, and the difference between the two
 746 scenarios decreases. As Da increases, diffusion becomes less important until the
 747 linear regime is reached, so that pulse and batch reactors behave similarly.

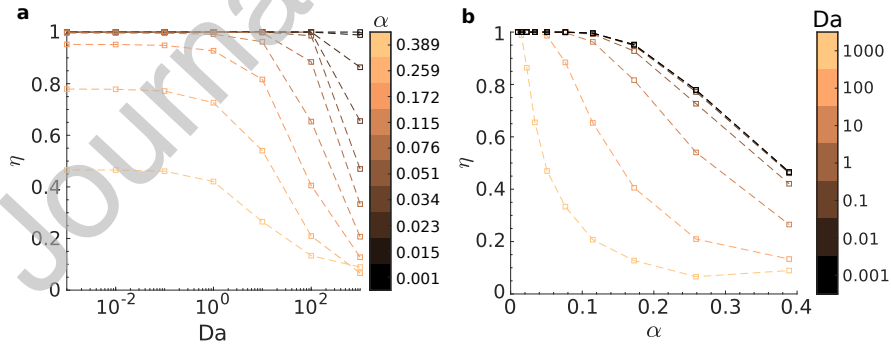


Figure A.12: Overall reaction enhancement η relative to the equivalent batch system. (a) Overall reaction enhancement as a function of Da for different α . (b) Overall reaction enhancement as a function of maximum batch rate α for different Damköhler numbers Da .

748 **Appendix B. Analytical solution for concentration in terms of bound-**
 749 **ary dynamics**

750 In this appendix, we provide details on the derivation of the concentration
 751 dynamics under diffusive transport, in terms of the boundary position $\xi(t)$ and
 752 the mass flux $f(t)$. The nondimensional dynamical equations for the saturated
 753 and linear regimes may be written as

$$\partial_t c_s(x, t) = \frac{\partial_x^2 c_s(x, t)}{2\text{Da}} - \alpha H[\xi(t) - |x|], \quad (\text{Appendix B.1a})$$

$$\partial_t c_\ell(x, t) = \frac{\partial_x^2 c_\ell(x, t)}{2\text{Da}} - c_\ell(x, t), \quad (\text{Appendix B.1b})$$

754 with the boundary conditions

$$c_s[\pm\xi(t), t] = c_\ell[\pm\xi(t), t] = \alpha, \quad (\text{Appendix B.2a})$$

$$\partial_x c_s(x, t)|_{x=\pm\xi(t)} = \partial_x c_\ell(x, t)|_{x=\pm\xi(t)} = \mp \text{Da} f(t) \quad (\text{Appendix B.2b})$$

755 and a given initial condition $c(x, 0)$.

756 We write $\hat{h}(k, t) = \int_{-\infty}^{\infty} dx \exp(-ikx)h(x, t)$ for the Fourier transform of a
 757 function h with respect to position, in terms of the Fourier variable k . Note
 758 that

$$\hat{c}_s(k, t) = \int_{|x| \leq \xi(t)} dx \exp(-ikx) c_s(x, t), \quad (\text{Appendix B.3a})$$

$$\hat{c}_\ell(k, t) = \int_{|x| > \xi(t)} dx \exp(-ikx) c_\ell(x, t), \quad (\text{Appendix B.3b})$$

759 and, according to the Leibniz rule for differentiation under the integral sign,

$$\int_{|x| \leq \xi(t)} dx \exp(-ikx) \partial_t c_s(x, t) = \partial_t \hat{c}_s(k, t) - 2\alpha \dot{\xi}(t) \cos[k\xi(t)], \quad (\text{Appendix B.4a})$$

$$\int_{|x| > \xi(t)} dx \exp(-ikx) \partial_t c_\ell(x, t) = \partial_t \hat{c}_\ell(k, t) + 2\alpha \dot{\xi}(t) \cos[k\xi(t)]. \quad (\text{Appendix B.4b})$$

760 Using these results, along with integration by parts for the spatial second
761 derivatives,

$$\partial_t \hat{c}_s(k, t) = -\frac{k^2 \hat{c}_s(k, t)}{2\text{Da}} - \hat{g}(k, t) - 2\alpha k^{-1} \sin[k\xi(t)], \quad (\text{Appendix B.5a})$$

$$\partial_t \hat{c}_\ell(k, t) = -\left(1 + \frac{k^2}{2\text{Da}}\right) \hat{c}_\ell(k, t) + \hat{g}(k, t), \quad (\text{Appendix B.5b})$$

762 where

$$\hat{g}(k, t) = f(t) \cos[k\xi(t)] - \frac{\alpha k \sin[k\xi(t)]}{\text{Da}}. \quad (\text{Appendix B.6})$$

763 Thus, in Fourier space, we obtain linear ordinary differential equations with the
764 boundary dynamics playing the role of a time-dependent forcing. The standard
765 form of the solutions is

$$\begin{aligned} \hat{c}_s(k, t) &= \hat{c}_s(k, 0) - \int_0^t du \exp\left[-\frac{k^2}{2\text{Da}}(t-u)\right] \\ &\quad \times \left[\hat{g}(k, u) + 2\alpha k^{-1} \sin[k\xi(u)] + 2\alpha \dot{\xi}(t) \cos[k\xi(u)]\right], \end{aligned} \quad (\text{Appendix B.7a})$$

$$\begin{aligned} \hat{c}_\ell(k, t) &= \hat{c}_\ell(k, 0) + \int_0^t du \exp\left[-\left(1 + \frac{k^2}{2\text{Da}}\right)(t-u)\right] \\ &\quad \times \left[\hat{g}(k, u) - 2\alpha \dot{\xi}(t) \cos[k\xi(u)]\right]. \end{aligned} \quad (\text{Appendix B.7b})$$

766 In order to obtain the total masses in each regime, it suffices to set $k = 0$, since
767 $M_{s,\ell}(t) = \hat{c}_{s,\ell}(0, t)$, see Eq. (Appendix B.3). This leads directly to Eq. (24) in
768 the main text.

769 Appendix C. Analytical solutions for asymptotic regimes

770 In this appendix, we identify and describe reaction- and diffusion-dominated
771 dynamical regimes. We obtain closed-form analytical solutions for the behavior
772 of the total mass under the weak coupling approximation introduced in section 4.

773 *Appendix C.1. Reaction-dominated dynamics*

774 If we neglect the effect of diffusion on the shape of the concentration profile,
775 we have $c_s(x, t) \approx c_R(x, t)$ for $|x| \leq \xi(t)$, where

$$c_R(x, t) = c(x, 0) - \alpha t = \frac{e^{-\frac{x^2}{2}}}{\sqrt{2\pi}} - \alpha t. \quad (\text{Appendix C.1})$$

776 Comparing to Eq. (32) for the shape of the profile, we see that we must require
777 $\text{Da} \gg \sigma$, so that diffusion effects may be neglected for the duration σ of the
778 saturated regime.

779 The approximate interface position is given by $\xi(t) \approx \xi_R(t)$, where

$$\xi_R(t) = \sqrt{-\ln [2\pi\alpha^2(1+t)^2]}. \quad (\text{Appendix C.2})$$

780 We thus have a duration of the saturated regime $\sigma \approx \sigma_R$ such that $\xi_R(\sigma_R) = 0$,
781 so that

$$\sigma_R = \frac{1 - \sqrt{2\pi\alpha^2}}{\sqrt{2\pi\alpha^2}}. \quad (\text{Appendix C.3})$$

782 For the diffusive flux, we have $f(t) \approx f_R(t)$, with

$$f_R(t) = \alpha \xi_R(t) \frac{1+t}{\text{Da}}. \quad (\text{Appendix C.4})$$

783 For consistency, we must also require $f(t) \ll 2\alpha\xi(t)$, so that the diffusive flux
784 from the saturated to the linear regime is negligible compared to the saturated
785 mass loss by reaction. This leads to the reaction-dominated condition

$$\text{Da} \gg \frac{1}{\sqrt{2\pi\alpha^2}}, \quad (\text{Appendix C.5})$$

786 which also ensures $\text{Da} \gg \sigma_R$.

787 For the saturated-regime mass, Eq. (35) becomes

$$M_s(t) \approx \text{erf} \left[\frac{\xi_R(t)}{\sqrt{2}} \right] - 2\alpha t \xi_R(t). \quad (\text{Appendix C.6})$$

788 For the linear-regime mass, neglecting the diffusive contribution $G(t)$ in Eq. (24b)
789 and using Eq. (27) for the initial mass, we have

$$M_\ell(t) \approx H(t) + \text{erfc} \left[\frac{\xi_R(0)}{\sqrt{2}} \right] e^{-t}. \quad (\text{Appendix C.7})$$

790 Integrating Eq. (25e) for $H(t)$ by parts, we obtain

$$H(t) \approx 2\alpha \left[\int_0^t du e^{-(t-u)} \xi_R(u) + \xi_R(0)e^{-t} - \xi_R(t) \right]. \quad (\text{Appendix C.8})$$

791 We are not aware of an exact closed-form solution, but a useful approximation
792 can be developed. Note that

$$\int_0^{\sigma_R} du e^{-(\sigma_R-u)} \xi_R(u) = \int_0^{1-\sqrt{2\pi\alpha^2}} du \frac{e^{-u/\sqrt{2\pi\alpha^2}}}{\sqrt{2\pi\alpha^2}} \sqrt{\ln \left[\frac{1}{(1-u)^2} \right]}. \quad (\text{Appendix C.9})$$

793 If $1 - \sqrt{2\pi\alpha^2} \ll 1$, we have $u \ll 1$ due to the integral bounds. If, on the other
794 hand, $\sqrt{2\pi\alpha^2} \ll 1$, we still have $u \ll 1$ for the dominant contributions due to
795 the exponential cutoff. Thus, we expand the logarithm for small u and obtain

$$\int_0^{\sigma_R} du e^{-(\sigma_R-u)} \xi_R(u) \approx \sqrt{2}(2\pi\alpha^2)^{1/4} \int_0^{\sigma_R} du e^{-u} \sqrt{u} \quad (\text{Appendix C.10})$$

$$\approx \frac{(2\pi\alpha^2)^{3/4}}{2\alpha} \left[\text{erf}(\sqrt{\sigma_R}) - 2e^{-\sigma_R} \sqrt{\frac{\sigma_R}{\pi}} \right], \quad (\text{Appendix C.11})$$

796 so that

$$H(\sigma_R) \approx (2\pi\alpha^2)^{3/4} \left[\text{erf}(\sqrt{\sigma_R}) - \sqrt{\frac{4\sigma}{\pi}} e^{-\sigma_R} \right] + 2\alpha \xi_R(0) e^{-\sigma_R}. \quad (\text{Appendix C.12})$$

797 It turns out this approximation works well for all values of α . A similar approach
798 yields

$$H(t) \approx 2\alpha \left(\xi_R(0) e^{-\sigma_R} - \xi_R(t) + \sqrt{\frac{2}{1+t}} e^{\frac{1+t}{2} \xi_R(t)^2} \left[\Gamma\left(\frac{3}{2}, \frac{1+t}{2} \xi_R(t)^2\right) - \Gamma\left(\frac{3}{2}, t + \frac{1+t}{2} \xi_R(t)^2\right) \right] \right), \quad (\text{Appendix C.13})$$

799 where $\Gamma(a, x) = \int_x^\infty dt t^{a-1} e^{-t}$ is the upper incomplete gamma function. This
800 approximation is somewhat less accurate for intermediate α values ($\alpha \sim 0.1$)

801 and intermediate times ($t \sim \sigma_R/2$). We also find the limiting forms

$$H(\sigma) \approx \begin{cases} (2\pi\alpha^2)^{3/4}, & \sqrt{2\pi\alpha^2} \ll 1 \\ \frac{2}{\sqrt{\pi}} (1 - \sqrt{2\pi\alpha^2})^{1/2}, & 1 - \sqrt{2\pi\alpha^2} \ll 1 \end{cases}. \quad (\text{Appendix C.14})$$

802 For the mass at the transition to the fully linear regime, we obtain

$$M_\ell(\sigma) = H(\sigma_R) + \operatorname{erfc} \left[\frac{\xi_R(0)}{\sqrt{2}} \right] e^{-\sigma_R}, \quad (\text{Appendix C.15})$$

803 with the limits

$$M_\ell(\sigma) \approx \begin{cases} (2\pi\alpha^2)^{3/4}, & \sqrt{2\pi\alpha^2} \ll 1 \\ \sqrt{2\pi\alpha^2}, & 1 - \sqrt{2\pi\alpha^2} \ll 1 \end{cases}. \quad (\text{Appendix C.16})$$

804 This leads to a reaction enhancement

$$\eta \approx \begin{cases} 1 - (8\pi^3)^{1/4} \sqrt{\alpha} e^{-(\sigma_B - \sigma_R)} \operatorname{erf}(\sqrt{\sigma_R}) \\ \quad - 2e^{-\sigma_B} \left[\xi_R(0) + \frac{\operatorname{erfc} \left[\frac{\xi_R(0)}{\sqrt{2}} \right]}{2\alpha} - (8\pi)^{1/4} \sqrt{\alpha\sigma_R} \right], & \alpha < 1/\sqrt{2\pi} \\ 1 - e^{-\sigma_B}/\alpha, & 1/\sqrt{2\pi} \leq \alpha < 1 \\ 0, & \alpha \geq 1 \end{cases}, \quad (\text{Appendix C.17})$$

805 which has the limiting behaviors

$$\eta \approx \begin{cases} 1 - (8\pi^3\alpha^2)^{1/4} e^{-\frac{\sqrt{2\pi}-1}{\sqrt{2\pi\alpha^2}}}, & \sqrt{2\pi\alpha^2} \ll 1 \\ 1 - \sqrt{2\pi} e^{-(\sqrt{2\pi}-1)} \left[1 - (\sqrt{2\pi}-1) (1 - \sqrt{2\pi\alpha^2}) \right] & 1 - \sqrt{2\pi\alpha^2} \ll 1 \\ 0, & \alpha \geq 1 \end{cases}. \quad (\text{Appendix C.18})$$

806 *Appendix C.2. Diffusion-dominated dynamics*

807 We now neglect the effect of reaction on the saturated-regime concentration
808 profile, which corresponds, for $|x| \leq \xi(t)$, to

$$c_s(x, t) \approx c_D(x, t) = \sqrt{\frac{\operatorname{Da}}{2\pi(\operatorname{Da} + t)}} e^{-\frac{\operatorname{Da} x^2}{2(\operatorname{Da} + t)}}. \quad (\text{Appendix C.19})$$

809 Taking into account that the lowest value of concentration in this regime is α ,
 810 comparison to Eq. (32) shows the approximation holds for $t \ll 1$. The position
 811 of the interface is now approximated by

$$\xi_D(t) = \sqrt{\frac{Da+t}{Da} \ln \left[\frac{Da}{2\pi\alpha^2(Da+t)} \right]}. \quad (\text{Appendix C.20})$$

812 From this, we find $\sigma \approx \sigma_D$, where

$$\sigma_D = Da \frac{1 - 2\pi\alpha^2}{2\pi\alpha^2}. \quad (\text{Appendix C.21})$$

813 The condition to ensure the validity of this regime for all relevant times is thus
 814 $\sigma_D \ll 1$. The diffusive flux is approximately given by

$$f_D(t) = \frac{\alpha\xi_D(t)}{Da+t}. \quad (\text{Appendix C.22})$$

815 In this case, the condition $2\alpha\xi(t) \ll f(t)$ that the reactive contribution to mass
 816 loss in the saturated regime be negligible compared to the diffusive contribution
 817 for all times $t < \sigma$ is thus $Da + \sigma_D \ll 1/2$. This leads to the diffusion-dominated
 818 condition

$$Da \ll \pi\alpha^2, \quad (\text{Appendix C.23})$$

819 which also ensures $\sigma_D \ll 1$,

820 The condition $\sigma_D \ll 1$ implies that the amount of reaction in the linear
 821 regime is negligible for $t < \sigma_D$. Thus, we find that $G(t) \approx F(t)$ and $H(t) \approx B(t)$.
 822 As expected for a diffusive profile, we obtain, for $t \leq \sigma_D$,

$$M_s(t) \approx \text{erf} \left[\frac{\xi_D(t)}{\sqrt{2}} \right], \quad (\text{Appendix C.24a})$$

$$M_\ell(t) \approx \text{erfc} \left[\frac{\xi_D(t)}{\sqrt{2}} \right], \quad (\text{Appendix C.24b})$$

823 so that $M_\ell(\sigma) \approx 1$ (no appreciable reaction). The corresponding reaction en-
 824 hancement is

$$\eta \approx \begin{cases} 1 - \frac{e^{-\sigma_B}}{\alpha}, & \alpha < 1 \\ 0, & \alpha \geq 1 \end{cases}. \quad (\text{Appendix C.25})$$

825 **Appendix D. Interface dynamics under the weak-coupling approxi-**
 826 **mation**

827 In this appendix, we assess the performance of the weak coupling approxi-
 828 mation in predicting the time evolution of the linear-saturated regime interface
 829 position $\xi(t)$ and the diffusive mass flux $f(t)$ between regimes. A comparison of
 830 the evolution of the interface position according to Eq. (33a) to full numerical
 831 simulations is shown in Fig. D.13. We show also the analytical solutions corre-
 832 sponding to the diffusive and reactive limits obtained in the previous appendix,
 833 Eqs. (Appendix C.20) and (Appendix C.2), respectively. In the limit of high
 834 Da , for all α , the numerical and semi-analytical solutions show good quanti-
 835 tative agreement and are also well approximated by the reaction-dominated
 836 solution. For high α , for all Da , Eq. (33a) also provides accurate predictions.
 837 It interpolates between the diffusion- and reaction-dominated at low and high
 838 Da , respectively, but differs substantially from both at intermediate Da . As ex-
 839 pected, low α leads to a worse quantitative approximation, except at high Da , for
 840 which the reaction-dominated approximation provides a good description. Note
 841 how low α and low Da lead to more complex dynamics, with a non-monotonic
 842 evolution of the interface position. This occurs because the interface evolution
 843 results from the competition of diffusion and reaction, with diffusion leading to
 844 both a widening and a reduction in the maximum of the concentration profile.
 845 Despite the worse quantitative agreement at low α , qualitative features such as
 846 non-monotonicity are well captured under the weak coupling approximation.

847 Figure D.14 shows a similar comparison for the diffusive flux $f(t)$ at the in-
 848 terface computed according to Eq. (33b). The diffusion- and reaction-dominated
 849 limits (Equations (Appendix C.22) and (Appendix C.4), respectively) are also
 850 shown. In this case, low Da or high α both lead to good quantitative agreement.
 851 When $Da \sim 1$ and α is low, the weak coupling solution predicts non-monotonic
 852 behavior, whereas numerical simulations show that the diffusive flux is more
 853 closely described by the monotonically-decreasing diffusion-dominated predic-
 854 tion at early times. Nonetheless, the weak coupling approximation captures

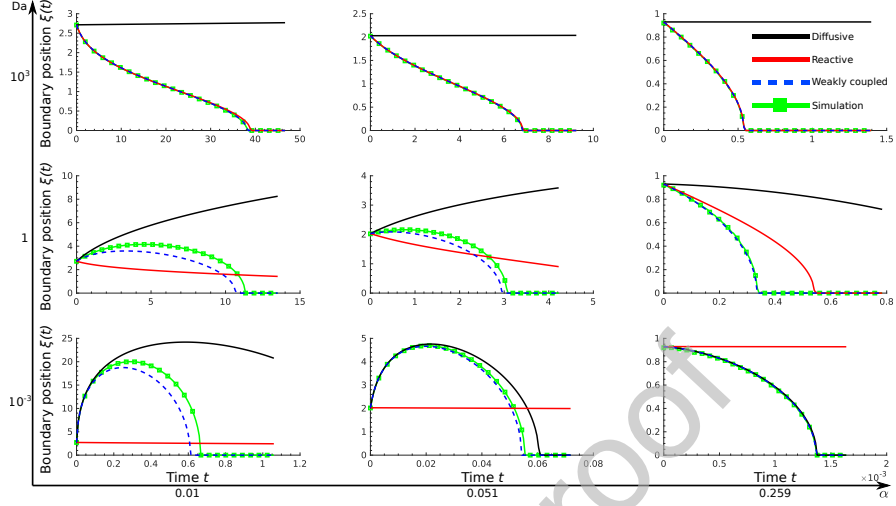


Figure D.13: Temporal evolution of the saturated-linear regime interface position. Analytical solutions for $\xi(t)$ in the diffusive and reactive limits are shown as solid black and red lines, respectively. The weak-coupling-based semi-analytical approximation is shown as a dashed blue line and the numerical simulations as a green line with square markers.

855 the transition time to fully linear kinetics well, whereas the diffusion-dominated
 856 approximation does not. Note that, as shown in Fig. D.15, the mass predictions
 857 at high Da are accurate, despite the quantitative deviations observed for $f(t)$ at
 858 low α . This is due to the fact that the magnitude of the diffusive flux is small
 859 in this limit, and therefore has a negligible effect compared to reaction.

860 Appendix E. Temporal derivatives of total mass

861 In this appendix, we present details on the calculation of the first and sec-
 862 ond derivatives of the total mass, Eq. (37). Taking the temporal derivative of
 863 Eq. (24), using the definitions in Eq. (25), we obtain

$$\dot{M}_s(t) = -2\alpha\xi(t) - f(t) + 2\alpha\dot{\xi}(t), \quad (\text{Appendix E.1a})$$

$$\dot{M}_\ell(t) = -M_\ell(0)e^{-t} - G(t) - H(t) + f(t) - 2\alpha\dot{\xi}(t). \quad (\text{Appendix E.1b})$$

864 Using Eq. (24b) for the linear-regime mass, the latter equation reads

$$\dot{M}_\ell(t) = -M_\ell(t) + f(t) - 2\alpha\dot{\xi}(t), \quad (\text{Appendix E.2})$$

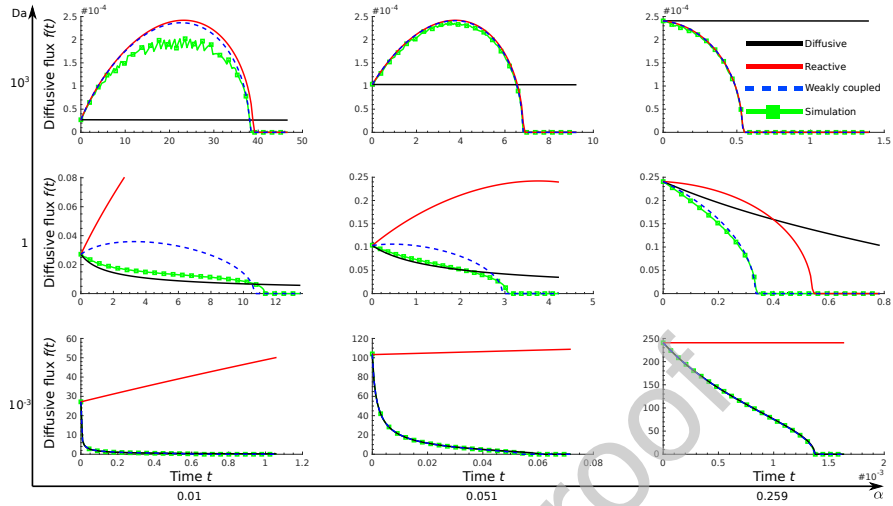


Figure D.14: Temporal evolution of the diffusive flux $f(t)$ at the saturated-linear regime interface. Results shown and color schemes are analogous to Fig. D.13.

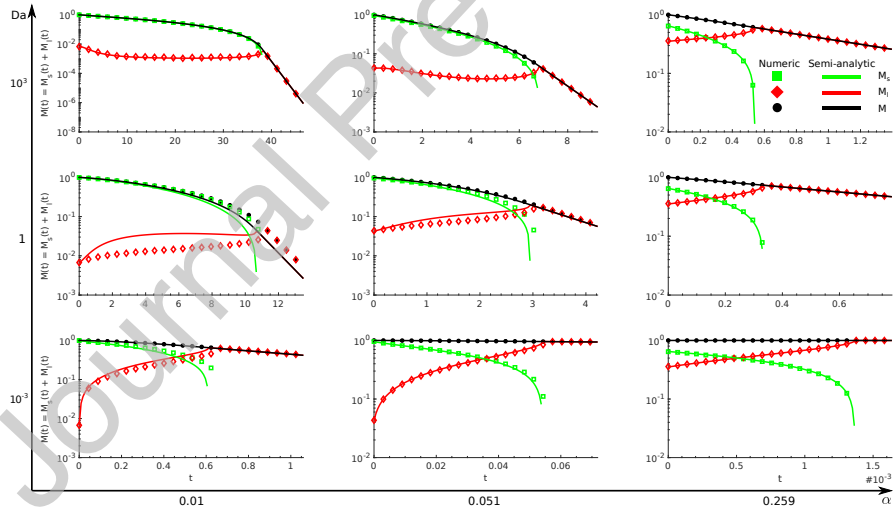


Figure D.15: Temporal evolution of total mass (black), mass in the saturated regime (green), and mass in the linear regime (red). The solid lines represent the weak-coupling approximation, and the markers are numerical simulations.

865 which has a simple interpretation: The first term characterizes the linear-regime
 866 reaction, the second refers to change in mass due to diffusive flux, and the third

867 quantifies the direct effect of boundary movement. Using Eq. (Appendix E.1a),
 868 this equation leads to

$$\dot{M}_\ell(t) + \dot{M}_s(t) = -M_\ell(t) - 2\alpha\xi(t), \quad (\text{Appendix E.3})$$

869 which, since $\dot{M} = \dot{M}_\ell + \dot{M}_s$, yields Eq. (37a) for the first time derivative of the
 870 total mass.

871 Next, we differentiate Eq. (37a), yielding

$$\ddot{M}(t) = -\dot{M}_\ell(t) - 2\alpha\dot{\xi}(t). \quad (\text{Appendix E.4})$$

872 Substituting Eq. (Appendix E.2) for $\dot{M}_\ell(t)$ leads to Eq. (37b).

873 **Appendix F. Simulations of reactive pulses with full Michaelis–Menten** 874 **kinetics**

875 In order to evaluate the effect of the piecewise linear approximation for
 876 the local reaction kinetics (equation (7)), we performed additional numerical
 877 simulations using the full Michaelis–Menten reaction kinetics (equation (6)).
 878 The temporal evolution of the mass with full Michaelis–Menten kinetics is found
 879 to be very close to the one simulated with the piecewise linear approximation
 880 (Fig. F.16.a). For low Da, the maximum reaction rate is slightly smaller than
 881 for the approximated kinetics and it occurs a bit earlier (Fig. F.16.b and F.16.c).
 882 The maximum reaction enhancement \tilde{r}_{\max} is however very similar for the full
 883 and approximated kinetics for a large range of Da and α (Fig. F.17).

884 **Appendix G. Simulations of three-dimensional reactive pulses**

885 In this Appendix, we investigate the sensitivity of our findings to dimension-
 886 ality. We thus consider a reactive pulse diffusing in three dimensions and solve
 887 numerically the reactive transport equation in spherical coordinates,

$$\frac{\partial c}{\partial t} = \frac{1}{2\text{Da}\rho^2} \frac{\partial}{\partial \rho} \left(\rho^2 \frac{\partial c}{\partial \rho} \right) + r(c), \quad (\text{Appendix G.1})$$

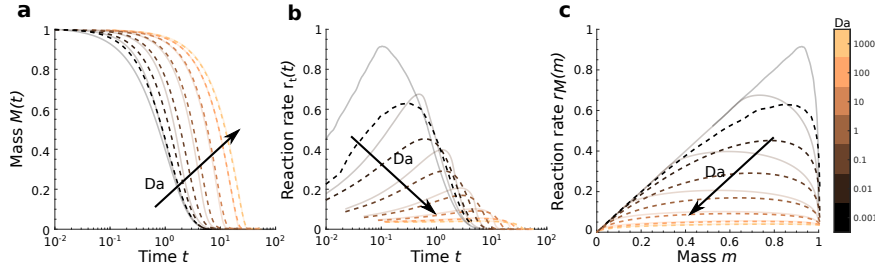


Figure F.16: Total mass and reaction rate computed numerically for the square initial condition and full Michaelis–Menten kinetics (equation (6)) with $\alpha = 0.05$ and Da ranging from 10^{-3} to 10^3 . The dashed lines represent the results of simulations with full Michaelis–Menten kinetics and the grey lines correspond to the piecewise linear kinetics presented in the paper. (a) Time evolution of total mass. (b) Time evolution of the reaction rate. (c) Reaction rate as a function of total mass.

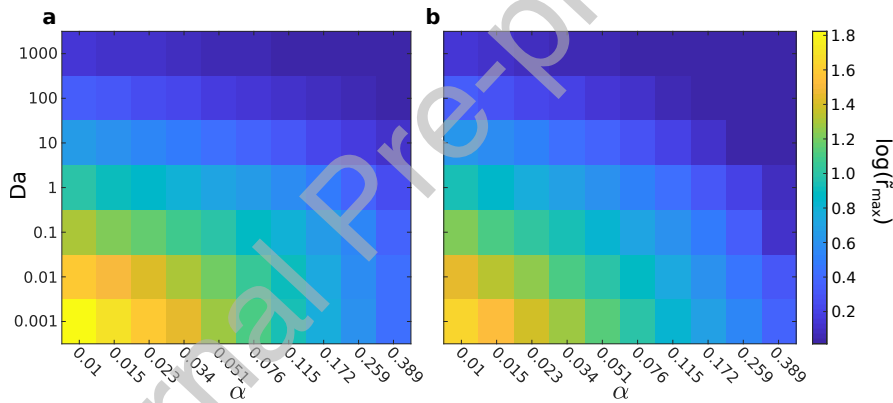


Figure F.17: Dependence of the maximum reaction enhancement \tilde{r}_{\max} on Da and α for (a) piecewise linear reaction kinetics (equation (7)) and (b) full Michaelis–Menten reaction kinetics (equation (6)).

888 with ρ the radial distance from the initial pulse of mass $M_0 = V_0 c_0 = 1$. The
 889 evolution of the mass and effective reaction rates is found to be similar for
 890 one-dimensional and three-dimensional pulses (Fig. G.18). In three-dimensions,
 891 the maximum reaction rate tends to be larger and to occur earlier (Fig. G.18.b
 892 and G.18.c). This is due to the fact that diffusion is more efficient at diluting
 893 a pulse in three-dimensions than in one-dimension. This enhanced diffusive

894 flux accelerates the transfer of mass from the saturated to the linear regime
 895 and thus tends to increase the effective reaction enhancement compared to one-
 896 dimensional pulses, with similar trends as a function of Da and α (Fig. G.19)
 897 .

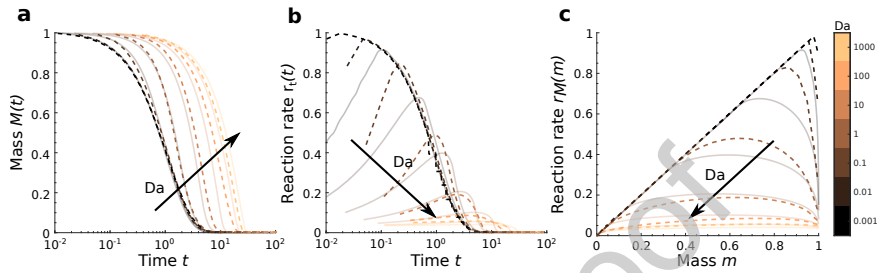


Figure G.18: Total mass and reaction rate computed numerically for three-dimensional and one-dimensional reactive pulses, with $\alpha = 0.05$ and Da ranging from 10^{-3} to 10^3 . The dashed lines represent the results of simulations of three-dimensional pulses (equation (Appendix G.1)) and the grey lines correspond to the results of simulations for one-dimensional pulses (equation (13)) presented in the paper. (a) Time evolution of total mass. (b) Time evolution of the reaction rate. (c) Reaction rate as a function of total mass.

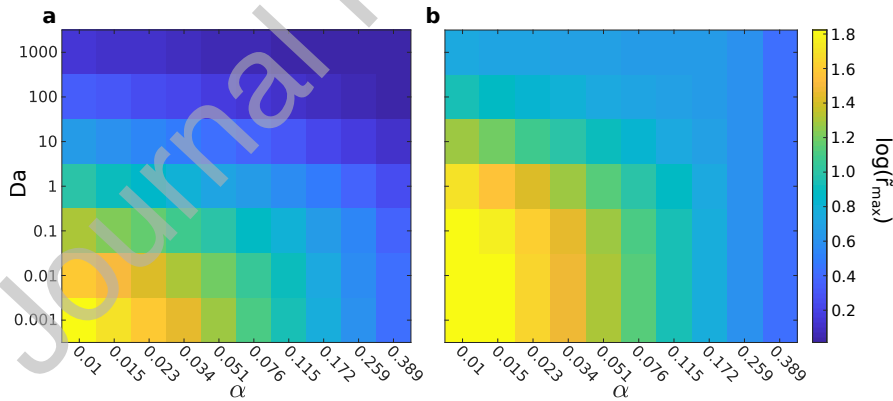


Figure G.19: Dependence of the maximum reaction enhancement \tilde{r}_{\max} on Da and α for (a) one-dimensional pulses (equation (13)) and (b) three-dimensional pulses (equation (Appendix G.1)).